Article
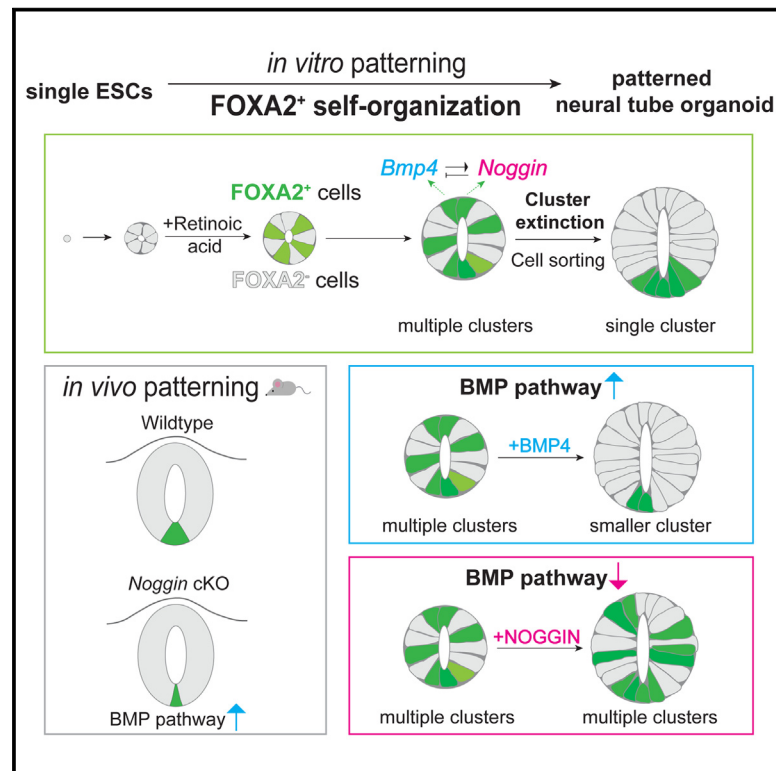
Mouse neural tube organoids self-organize floorplate through BMP-mediated cluster competition

Graphical abstract

Highlights

- During neural tube organoid self-organization, scattered FOXA2+ cells form clusters

- FOXA2+ clusters compete via long-range signaling to establish a "winning" floorplate

- BMP4 and NOGGIN control numbers and sizes of FOXA2+ clusters

- NOGGIN is functionally involved in controlling floorplate size *in vivo*

Authors

Teresa Krammer, Hannah T. Stuart, Elena Gromberg, ..., James Briscoe, Anna Kicheva, Elly M. Tanaka

Correspondence

elly.tanaka@imba.oeaw.ac.at

In brief

Krammer et al. show that retinoic-acid-triggered self-organization of neural tube organoids occurs via induction of scattered FOXA2-expressing cells that undergo clustering and competition to persist and form floorplates. Cluster competition occurs via BMP signaling, which controls floorplate number and size *in vitro* and size *in vivo* at the mid/hindbrain region.

CellPress

Article

Mouse neural tube organoids self-organize floorplate through BMP-mediated cluster competition

Teresa Krammer,[1,2,8,9] Hannah T. Stuart,[1,3,8,9] Elena Gromberg,[1,2,8] Keisuke Ishihara,[1,10] Dillon Cislo,[4] Manuela Melchionda,[3] Fernando Becerril Perez,[1,2,9] Jingkui Wang,[1,9] Elena Costantini,[1,9] Stefanie Lehr,[5] Laura Arbanas,[1] Alexandra Hörmann,[6] Ralph A. Neumüller,[6] Nicola Elvassore,[7] Eric Siggia,[4] James Briscoe,[3] Anna Kicheva,[5] and Elly M. Tanaka[1,9,11,*]

[1]Research Institute of Molecular Pathology (IMP), Vienna BioCenter (VBC), Campus-Vienna-Biocenter 1, 1030 Vienna, Austria
[2]Vienna BioCenter PhD Program, Doctoral School of the University of Vienna and Medical University of Vienna, 1030 Vienna, Austria
[3]The Francis Crick Institute, London, UK
[4]Center for Studies in Physics and Biology, The Rockefeller University, New York, NY, USA
[5]Institute of Science and Technology Austria (ISTA), Klosterneuburg, Austria
[6]Boehringer Ingelheim RCV GmbH & Co KG, Vienna, Austria
[7]Department of Industrial Engineering, University of Padova & Veneto Institute of Molecular Medicine (VIMM), Padova, Italy
[8]These authors contributed equally
[9]Present address: Institute of Molecular Biotechnology of the Austrian Academy of Sciences (IMBA), Vienna BioCenter, Dr. Bohr-Gasse 3, 1030 Vienna, Austria
[10]Present address: University of Pittsburgh, Pittsburgh, PA, USA
[11]Lead contact
*Correspondence: elly.tanaka@imba.oeaw.ac.at
https://doi.org/10.1016/j.devcel.2024.04.021

SUMMARY

During neural tube (NT) development, the notochord induces an organizer, the floorplate, which secretes Sonic Hedgehog (SHH) to pattern neural progenitors. Conversely, NT organoids (NTOs) from embryonic stem cells (ESCs) spontaneously form floorplates without the notochord, demonstrating that stem cells can self-organize without embryonic inducers. Here, we investigated floorplate self-organization in clonal mouse NTOs. Expression of the floorplate marker FOXA2 was initially spatially scattered before resolving into multiple clusters, which underwent competition and sorting, resulting in a stable "winning" floorplate. We identified that BMP signaling governed long-range cluster competition. FOXA2+ clusters expressed BMP4, suppressing FOXA2 in receiving cells while simultaneously expressing the BMP-inhibitor NOGGIN, promoting cluster persistence. *Noggin* mutation perturbed floorplate formation in NTOs and in the NT *in vivo* at mid/hindbrain regions, demonstrating how the floorplate can form autonomously without the notochord. Identifying the pathways governing organizer self-organization is critical for harnessing the developmental plasticity of stem cells in tissue engineering.

INTRODUCTION

During vertebrate development, groups of cells called organizers secrete morphogens to induce cell fate patterning in the surrounding tissues.[1,2] In the embryo, organizers are induced by interactions between emerging tissues (reviewed in[3]). Correct organizer placement relies on pre-existing asymmetries in the embryo and the delivery of polarizing cues. Intriguingly, recent discoveries *in vitro* have found that organizers can form by a process of self-organization in the absence of their natural developmental inducers.[4–7] Despite their central importance for multicellular development as well as tissue regeneration and engineering, the mechanisms by which organizers self-organize are poorly understood.

The neural tube (NT) is the embryonic precursor of the central nervous system. Patterning of neural progenitor identities along the body axes ensures the formation of the correct diversity and arrangement of neurons.[8,9] In the developing spinal cord, NT patterning along the dorsal-ventral axis is guided by two opposing organizers: the dorsal roofplate, secreting bone morphogenetic proteins (BMPs) and Wingless/Integrated (WNTs), and the ventral floorplate, secreting Sonic Hedgehog (SHH) morphogen.[10–13] *In vivo*, the ventral floorplate organizer is usually induced by SHH and other signals from the underlying notochord,[14,15] which has been most extensively studied at thoracic levels. The more anterior floorplate is induced earlier during amniote gastrulation[14,16,17] and forms independently of notochord signaling by a mechanism that is currently unclear.
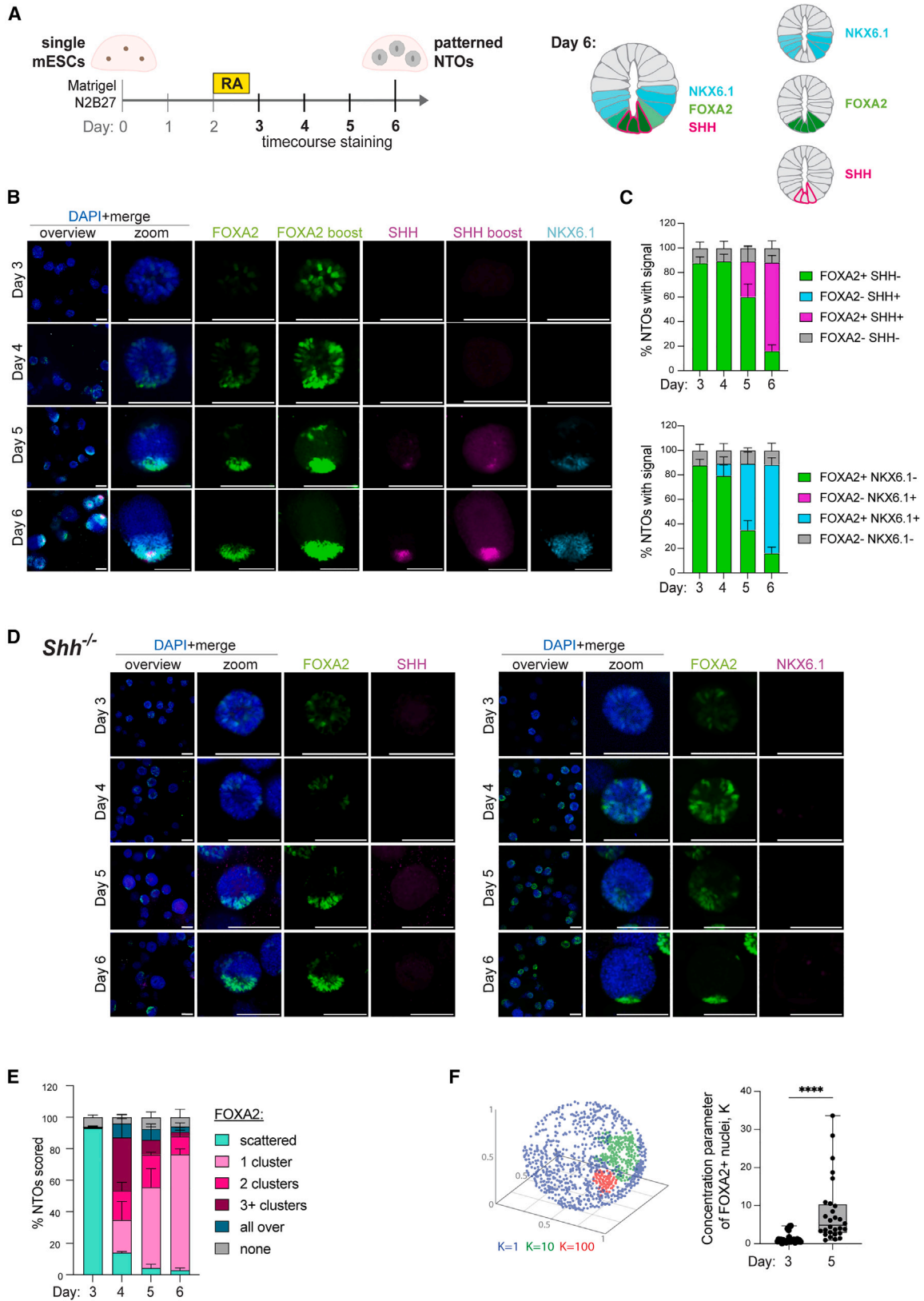
(legend on next page)

The SHH-expressing floorplate has been shown to self-organize in NT organoids (NTOs) *in vitro*[6] in the absence of notochord or any directional inductive cues. NTOs form clonally, by differentiating single mouse embryonic stem cells (ESCs) embedded in three-dimensional (3D) hydrogels,[6,18] resulting in neuroepithelial cysts with a single apical lumen that exhibit a "default" dorsal midbrain identity. A global pulse of retinoic acid (RA) applied at day 2 for 18 h posteriorizes NTOs to hindbrain levels and triggers self-organization of dorsal-ventral patterning by day 6[6] (Figures 1A and S1A). This phenomenon is characterized by the formation of a localized FOXA2+SHH+ floorplate at the emergent ventral pole, which then drives ventral-to-dorsal patterning of neural progenitor identities. Here, we address the mechanism governing the self-organization of this floorplate organizer in NTOs.

RESULTS

FOXA2+ floorplate precursors self-organize from a spatially scattered to a clustered state in clonal NTOs

To characterize the spatiotemporal dynamics of how the FOXA2+SHH+ floorplate self-organizes in mouse NTOs, we first performed time course immunofluorescence (IF) staining after RA pulse (Figure 1A). We assayed FOXA2, SHH, and SHH/GLI-responsive NKX6.1 (Figure 1B) and quantified the number of NTOs expressing each marker (Figure 1C). Temporally, FOXA2 expression was observed from day 3 onward in >80% of NTOs prior to detection of SHH or NKX6.1 proteins. From days 5 to 6, the number of NTOs with FOXA2 and detectable SHH/NKX6.1 increased, whereas SHH or NKX6.1 expression was not observed in FOXA2− NTOs (Figure 1C), indicating that FOXA2 preceded SHH expression and activity. Accordingly, RNA sequencing (RNA-seq) analysis[19] showed upregulation of the *FoxA2* transcript earlier than *Shh* or *Nkx6.1* (Figure S1B) and confirmed the expected regional identity of the NTOs, consistent with previous findings by Meinhardt et al.[6] IF and RNA-seq both showed an increase in the level of FOXA2 expression over time from day 3 onward (Figures 1B and S1B).

In vivo, SHH from the notochord can induce floorplate FOXA2 expression via GLI binding sites found in FOXA2 regulatory elements.[15,20] Although we observed FOXA2 expression prior to SHH in NTOs (Figures 1B, 1C, S1B, and S1C), we nonetheless asked whether genetic deletion of SHH would abolish FOXA2 induction and cluster formation. NTOs formed from *Shh*−/− ESCs showed no detectable SHH or NKX6.1 expression at any time point (Figures 1D and S1C). However, FOXA2 induction and cluster formation still occurred in *Shh*−/− NTOs (Figures 1D and S1D). Unlike parental wild-type (WT) NTOs, the proportion of *Shh*−/− NTOs exhibiting FOXA2 expression decreased from 80% to 60% over days 5–6 (Figure S1C), suggesting a role for SHH in FOXA2 maintenance at later time points, consistent with phenotypes of prolonged SHH antagonism in NTOs[6] and the SHH-driven regulatory architecture at the *FoxA2* locus.[20]

Spatially, NTOs expressed FOXA2 at day 3 in a scattered, salt-and-pepper manner (Figure 1B). Subsequently, the FOXA2 signal became increasingly clustered until, by days 5–6, FOXA2 was found in discrete domains inside which SHH expression commenced to yield a functional floorplate, reflected by induction of NKX6.1 (Figures 1B and 1C). Over time, the proportion of NTOs with scattered FOXA2, versus 3+, 2, or 1 cluster per NTO, shifted until a majority of NTOs contained a single FOXA2+ cluster (Figure 1E). To quantify the spatial distribution of FOXA2+ nuclei in 3D, we performed von Mises-Fisher analysis in which a concentration parameter *K* is computed, based on the sum of directional vectors from the NTO center, to describe how tightly the vectors are distributed around their average orientation. This confirmed that FOXA2 expression became increasingly concentrated over time (Figure 1F). Together, this shows that floorplate self-organization in RA-treated NTOs is characterized by "salt-and-pepper" FOXA2 induction, followed by clustering of FOXA2+ floorplate precursor cells, which occurs prior to and independently of SHH expression.

Intermediate FOXA2+ clusters interact via competition and sorting during self-organization

We next sought to understand whether and how individual NTOs progress from scattered to multi-cluster to single floorplates. We generated a FOXA2-Venus fusion reporter at the endogenous locus, together with knockin of H2A-mCherry into the safe-harbor *Rosa26* locus to constitutively label nuclei

Figure 1. Clonal NTOs transition from a scattered expression of FOXA2+ cells to a clustered state, which can occur in the absence of SHH

(A) Schematic of NTO formation. Single ESCs form epithelial NTOs within 2 days in Matrigel and N2B27. An 18 h pulse of retinoic acid induces floorplate formation and dorsoventral patterning at the endpoint day 6.

(B) IF time course of NTOs fixed from days 3 to 6 showing (from left to right, single *z* slice) a merged overview image at 10× magnification, a representative NTO (zoom) stained for DAPI (blue), and the dorsoventral patterning markers FOXA2 (green), SHH (magenta), and NKX6.1 (cyan). In the second FOXA2 column, FOXA2 images were scaled with lower maximal grayscale value to highlight the early spatial pattern. In the second SHH column, the same metric was applied. Scale bars, 100 μm.

(C) Quantification of marker expression in (*n* = 528) NTOs over time. Colored bars correspond to staining in (B) (*n* = 192 for day 3, *n* = 158 for day 4, *n* = 134 for day 5, and *n* = 44 for day 6).

(D) *Shh*−/− NTOs undergo FOXA2-cell clustering. Time course of *Shh*−/− NTOs fixed from days 3 to 6 showing (from left to right, single *z* slice) a merged overview image at 10× magnification, a representative NTO (zoom) stained for DAPI (blue), and the dorsoventral patterning markers FOXA2 (green) and SHH or NKX6.1 (magenta). For parental control, see Figure S1. Scale bars, 100 μm.

(E) FOXA2+ cell cluster distribution over time. FOXA2 spatial distribution was classified into "scattered," "1 cluster," "2 clusters," "3 or more clusters," "none" (FOXA2−), or "all over" (almost entirely FOXA2+). A total of 1,148 NTOs were manually analyzed (*n* = 292 for day 3, *n* = 285 for day 4, *n* = 209 for day 5, and *n* = 362 for day 6).

(F) FOXA2+ cell clustering analysis using von Mises-Fisher parameter. Left: schematic illustrating quantitative clustering parameter (*K*, from von Mises-Fisher). Right: von Mises-Fisher analysis of 3D FOXA2+ cell distribution in day 3 (*n* = 27) and day 5 (*n* = 28) NTOs. By day 5, FOXA2-expressing cells show a higher *K* value. Each dot represents the *K* value of a single NTO. Results were statistically analyzed using a Mann-Whitney test with *p* ≤ 0.0001. Error bars show standard deviation (SD), and asterisks mark statistical significance.
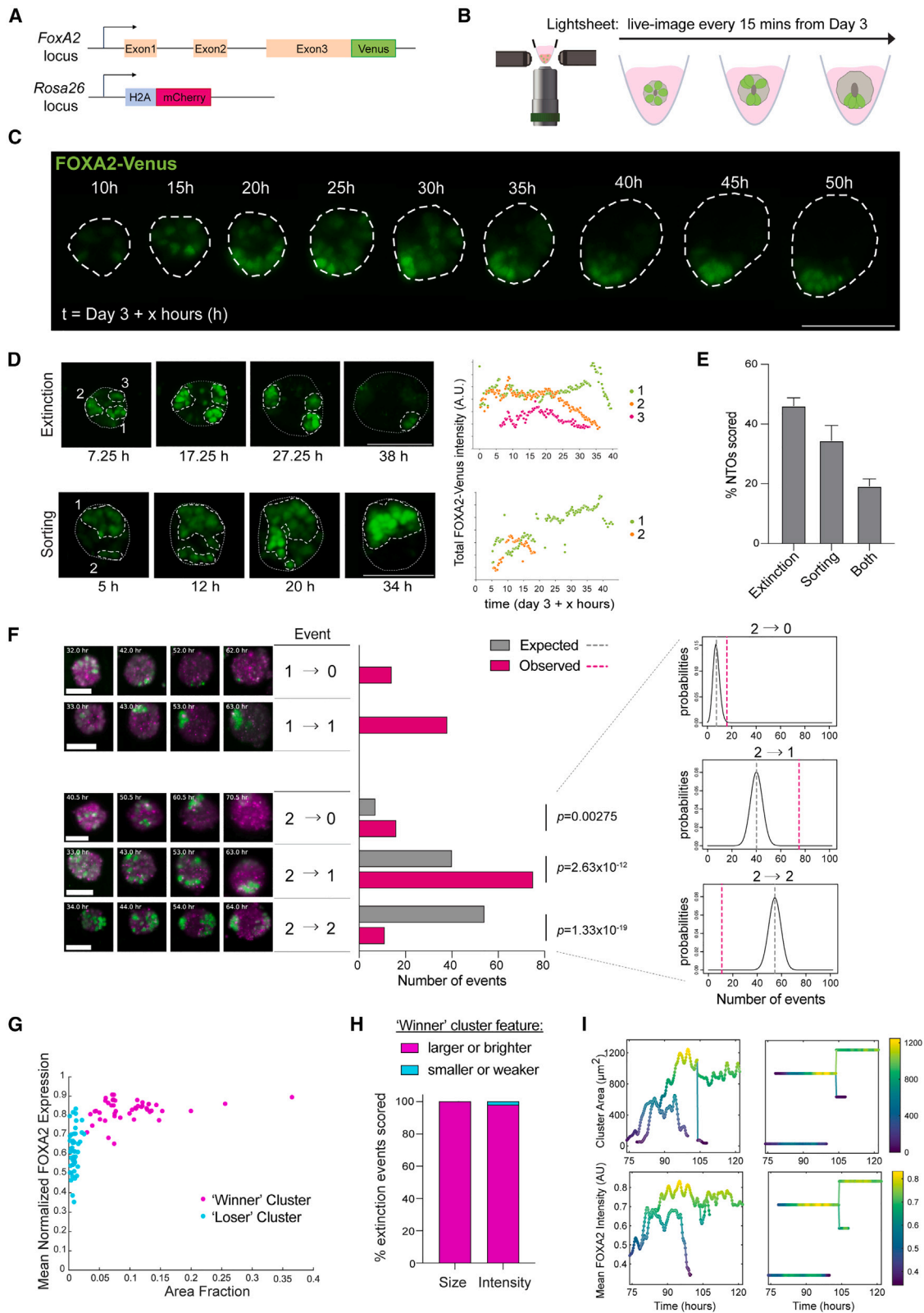
See also Figure S1.

Figure 2. Statistical analysis and tracking of live cluster dynamics reveal cluster competition during self-organization

(A) Schematic of double reporter generation. Venus was knocked in after the 3rd exon at the C terminus of the endogenous *FoxA2* locus, generating a fusion protein. In addition, an H2A-mCherry construct was knocked into the ubiquitously expressed Rosa26 locus to mark nuclei.

(legend continued on next page)

(Figures 2A and S2A–S2C). Using 3D light-sheet live imaging, we acquired images every 15 min starting from day 3 in over 300 live NTOs (Figure 2B). This revealed self-organization of FOXA2-Venus^{+} cells from a spatially scattered to a clustered state via progressive formation of and resolution between intermediate clusters (Figure 2C; Video S1), in agreement with fixed sample quantifications (Figure 1E).

We observed two distinct modes by which intermediate clusters resolved (Figure 2D; Videos S2 and S3): (1) cluster extinction, whereby FOXA2-Venus expression was lost in some clusters while it persisted in others, and (2) physical cell-sorting, whereby FOXA2-Venus^{+} cells from one cluster coalesced with another cluster. These two behaviors were not mutually exclusive: 20% of NTOs exhibited both sorting and extinction of FOXA2-Venus[+] clusters, while 35% and 45% exhibited only sorting or only extinction, respectively (Figure 2E). Because a switch from E- to N-cadherin is observed during neural differentiation from mouse ESCs,[6,18] we examined whether there was differential expression of these cell adhesion molecules between FOXA2^{+} and FOXA2^{−} cells. We observed E-cadherin expression in FOXA2^{+} versus N-cadherin expression in FOXA2^{−} cells from day 4 onward, which could explain the sorting behavior (Figures S2D–S2G). Here, however, we focused further on cluster extinction, as it was observed in the majority of NTOs.

To understand whether cluster extinction occurred autonomously or via communication (competition) between clusters, we categorized live-imaged NTOs according to the number of FOXA2-Venus[+] clusters observed at intermediate versus endpoint times. We then tested statistically whether clusters behaved independently of each other. For NTOs with one intermediate cluster, 14 out of 52 extinguished that cluster during self-organization (Figure 2F). By considering the disappearance of a given cluster as a process with this observed probability (0.269), we formulated the null hypothesis that, if FOXA2-Venus[+]

clusters behave independently, the expected outcome for NTOs with two intermediate clusters losing one or both clusters would be 0.393 or 0.072, respectively. We compared these expected outcomes with experimental observations (Figure 2F). In live-imaged NTOs with two intermediate clusters, the observed outcomes differed significantly from the expected outcomes. A cluster was significantly more likely to be extinguished if another cluster was present (Figure 2F), indicating competitive communication between the clusters that governs final outcome.

We aimed to investigate whether there are quantitative features that can predict which cluster will persist and which will be extinguished in competition. To relate cluster features, such as size and FOXA2 intensity, at intermediate time points versus their subsequent outcomes, we established a semi-automated cluster identification pipeline to track FOXA2-Venus[+] clusters over time in live-imaged NTOs in 3D. We performed a detailed analysis on a representative set of movies in which cluster extinction events were observed (20 NTOs comprising 47 extinction events) (Figures 2G–2I, S2H, and S2I; Table S1). When considering the relative properties of clusters in a given NTO 1 h prior to each extinction event, the winning cluster was always larger, occupying >5% of the surface area of the whole NTO (Figures 2G and 2H; Table S1). The winning cluster also exhibited a higher mean FOXA2 intensity in each comparison, except in one case (Figure 2H; Table S1), at the time analyzed. Before that, size and intensity were somewhat predictive of cluster persistence (Figure S2I).

BMP signaling activity anti-correlates with FOXA2 expression during cluster interaction

We sought to determine the molecular signals that facilitate cluster communication. To identify candidates, we performed bulk RNA-seq of sorted FOXA2-Venus[+] versus FOXA2-Venus^{−} cells at day 5, a time point at which cluster extinction was occurring (Figures 3A and S3A). Reasoning that secreted signals could explain

(B) Schematic (created with BioRender) of timelapse imaging of double reporter on the Viventis lightsheet microscope. Full image stacks with 3 μm *z* step size were taken every 15 min starting 6 h post RA removal on day 3 for 48–75 h.

(C) Images from timelapse series of an NTO (maximum-intensity *z*-projections), following the spatial organization of FOXA2 (green) over 50 h showing self-organization from a dispersed (salt-and-pepper) into a clustered state (see Video S1). Dashed white lines mark the outlines of the NTO. Scale bars, 100 μm.

(D) Two distinct modes of cluster formation. Selected maximum-intensity *z*-projection images from two (upper and lower) NTO timelapse series. Upper: "extinction": three FOXA2^{+} (green) clusters form, and then one remains while two disappear (see Video S2). Lower: "sorting": two distinct clusters grow and coalesce into a single cluster over time (see Video S3). Right: cluster intensities were tracked over time in graphs. Dotted gray lines mark the outlines of NTOs, dashed white lines mark the outline of FOXA2^{+} clusters. Scale bars, 100 μm.

(E) A total of *n* = 93 NTOs from three different timelapses that displayed as 2 → 1 behavior were subclassified into their mode of self-organization (extinction, sorting, or both), taking into account that sorting might be overestimated due to analysis using maximum-intensity *z*-projections.

(F) Left: representative time course images for each category, shown as maximum-intensity *z*-projections; scale bars, 50 μm, and scoring of NTOs according to FOXA2-Venus[+] cluster numbers at intermediate versus endpoint times. Middle: based on the frequency of cluster disappearance in NTOs with one intermediate cluster (*n* = 52), the expected outcomes (gray) for NTOs with 2 intermediate clusters (*n* = 102) were calculated using binomial distribution assuming independent cluster behavior, then compared with observed outcomes (magenta). Right: calculation of *p* values based on the binomial distribution for each case, with the expected value indicated by gray lines and the observed numbers by magenta lines.

(G) Measurement of FOXA2 area fraction and mean normalized FOXA2 expression in each cluster, averaged over 1 h time before a cluster was extinguished ("loser" clusters, cyan) versus clusters that persisted (winner clusters, magenta) from movie analyses performed as shown in Figure S2H. A two-sample Kolmogorov-Smirnov (KS) test was used to assess whether the cluster area fraction and the mean normalized cluster FOXA2 expression of the persisting and extinguished clusters were drawn from the same population. This null hypothesis was rejected both for the area fraction data (KS statistic = 1, *p* value 4.7e−22) and the mean FOXA2 expression data (KS statistic = 0.81, *p* value 1.5e−14).

(H) For each extinction event, the comparative properties of the persisting winning versus extinguished losing cluster in that NTO are classified.

(I) Topology and features of dynamical FOXA2^{+} cluster tracking showing cluster area (upper panel) and mean FOXA2 intensity (lower panel). Results shown are drawn from a single NTO with multiple clusters. Left: dynamical cluster property over time. Right: topology of the directed acyclic graph (DAG) describing the cluster tracking. The *y* axes of the right plots have no physical meaning and are formatted to provide a clear visual separation between connected components of the DAG.

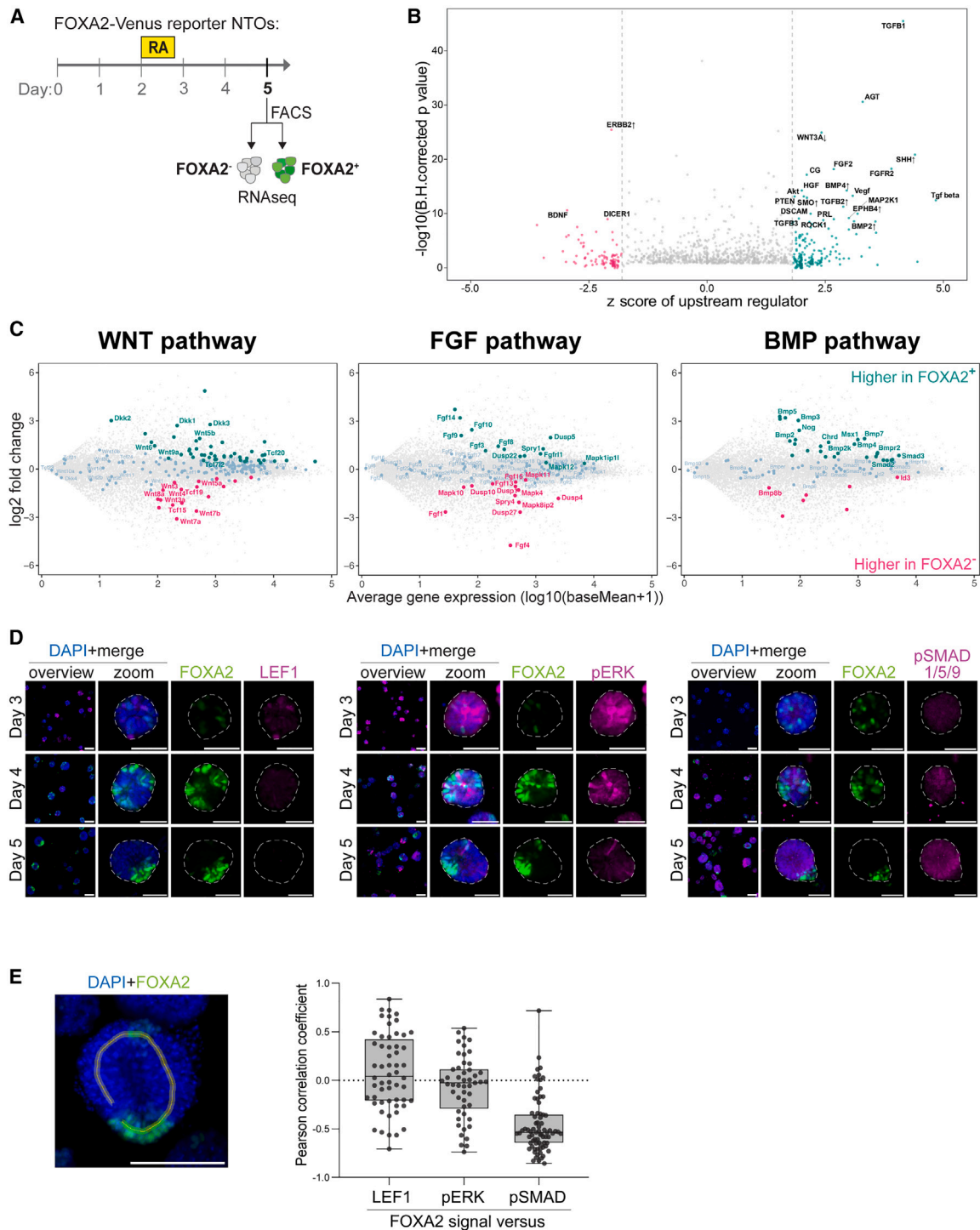See also Figure S2 and Videos S1, S2, and S3.

Figure 3. FOXA2$^+$ cells express *BMP*s and *Noggin*, while FOXA2$^-$ cells display a higher pSMAD1/5/9 signal

(A) Schematic of RNA-seq performed on sorted FOXA2$^+$ and FOXA2$^-$ cell populations of day 5 NTOs made from the reporter cell line.

(B) Activity plot of upstream regulators predicted to be activated or inhibited based on the observed expression changes in FOXA2$^+$ versus FOXA2$^-$ cells. Regulators are colored based on activation *Z* score at a threshold of 1.8, and the top 20 candidates based on significance are labeled; an arrow next to a regulator name indicates significant up- or downregulation of the gene in FOXA2$^+$ (versus FOXA2$^-$).

(C) WNT, FGF, and BMP pathway members showing differential gene expression between FOXA2$^+$ and FOXA2$^-$ cells. MA plot of the RNA-seq data showing log$_2$ fold changes of genes over their average gene expression against samples (*y* axis: FOXA2$^+$ versus FOXA2$^-$ log ratio values, *x* axis: log$_{10}$(baseMean + 1) of average gene expression). Color highlights genes assigned to either WNT signaling pathway (GO: 0016055), FGF signaling pathway (GO: 0008543), or BMP signaling

(legend continued on next page)

long-range mutual inhibition between clusters, we focused on the expression of ligands, receptors, transducers, and modulators for the major secreted signaling pathways. Using two methods to test enrichment of signaling pathway signatures in FOXA2$^+$ versus FOXA2$^-$ cells (Figures 3B and S3B), signatures of WNT, fibroblast growth factor (FGF), and BMP signaling were uncovered in FOXA2$^+$ cells. Various WNT and FGF ligands were expressed in FOXA2$^+$ or FOXA2$^-$ populations (Figure 3C). Notably, BMP ligands were almost exclusively expressed in FOXA2$^+$ cells (Figure 3C). Expression of the secreted WNT inhibitors *Dkk1-3* and secreted BMP inhibitors *Noggin* and *Chordin* was enriched in FOXA2$^+$ cells, whereas FGF-responsive *Spry4* was enriched in FOXA2$^-$ cells (Figure 3C). We therefore investigated WNT, FGF, and BMP pathways in NTOs by spatial analyses of signaling activities and functional perturbations, as described below.

To functionally test the candidate pathways, we performed pharmacological screens using small molecules and recombinant proteins to activate or inhibit WNT, FGF, or BMP signaling from days 3 to 5 (Figure S3C). WNT or FGF perturbations led to a slight decrease in the percentage of FOXA2$^+$ NTOs at day 5, irrespective of whether the pathway was activated or inhibited. However, BMP activation decreased—while inhibition increased—the percentage of FOXA2$^+$ NTOs, demonstrating that the level of BMP signaling modulates FOXA2 expression.

To assess the activities of the WNT, FGF, and BMP pathways during cluster self-organization in NTOs, we assayed for LEF1, phosphorylated (p)ERK, or pSMAD1/5/9, respectively, by IF (Figure 3D). LEF1 and pERK signal decreased, whereas pSMAD1/5/9 increased, from days 3 to 5, suggesting an increase in BMP pathway activity after RA treatment. Interestingly, we observed that the pSMAD1/5/9 signal predominated in FOXA2$^-$ cells compared with FOXA2$^+$ cells (Figures 3D, S3D, and S3E). To measure the degree of spatial correlation between FOXA2 expression versus WNT, FGF, or BMP signaling activities, we measured signal intensities along a line that bisected cells in NTOs, circling the lumen, then computed the Pearson correlation coefficients between FOXA2 and LEF1, pERK, or pSMAD1/5/9 signals, respectively (Figure 3E). We did not observe any type of correlation between FOXA2 and LEF1 or pERK signal. By contrast, a negative correlation was found between FOXA2 and pSMAD1/5/9 intensities, consistent with a role of BMP signaling in FOXA2 suppression. Taken together, the BMP pathway exhibited an appropriate activity pattern and perturbation phenotype to be further considered as a candidate signal by which intermediate FOXA2$^+$ clusters interact.

BMP signaling regulates FOXA2 cluster resolution
To functionally investigate the role of BMP signaling during the phase of cluster competition, we perturbed the BMP pathway

from day 4 onward using pharmacological and genetic approaches (Figure 4A). To quantitatively assess the effect of perturbations on inter-cluster communication, we adapted our protocol to support the growth of larger NTOs (Figures S4A–S4C). These demonstrated a higher frequency of multiple rather than single FOXA2$^+$ clusters (Figure S4D) due to a positive correlation between NTO size and endpoint cluster number (Figure S4E).

BMP4 ligand treatment led to a dose-dependent decrease in the proportion of NTOs with any FOXA2$^+$ clusters persisting at day 6 (Figures 4B and 4C). Conversely, BMP pathway inhibition by application of recombinant NOGGIN or the small molecule LDN193189 (LDN) led to a mild increase in the total proportion of NTOs with any FOXA2$^+$ clusters (Figures 4B, 4C, and S3E). When broken down into whether each NTO contained 1, 2, or 3+ clusters, BMP inhibition resulted in a significant increase in the proportion of NTOs with 3+ endpoint clusters (Figure 4C). This is consistent with a role of endogenous BMP signaling in promoting FOXA2 cluster extinction, which is alleviated by BMP inhibition.

Given that larger and brighter clusters were more likely to persist (Figures 2G and 2H), we hypothesized that heterogeneous expression in BMP pathway genes as a function of FOXA2 expression levels may contribute to the competition. Using fluorescence-activated cell sorting (FACS), we sorted cells from NTOs according to their FOXA2-Venus levels into negative, low, medium, and high expression at day 4 and performed RNA-seq. Indeed, we observed an increase in expression of BMP ligands as well as inhibitors, corresponding to higher FOXA2 expression levels (Figure S4F). When analyzing expression in FACS-sorted FOXA2-Venus negative, low, medium, and high cells from intermediate (day 4) and clustered (day 5) NTOs, we found that by day 5 the tested BMP ligands, as well as inhibitors, showed positive correlation with FOXA2 expression levels or increased expression in FOXA2$^+$ compared with negative cells, which could explain why brighter FOXA2$^+$ clusters are more likely to "win" the competition (Figure S4G).

We then tested whether endogenously produced NOGGIN plays a role in regulating FOXA2$^+$ clusters in NTOs by generating *Noggin* mutant (*Nog^{mut}*) ESCs with CRISPR-Cas9 (Figure S4H), then subjecting them to NTO formation and BMP pathway perturbations (Figures 4D–4F). A significantly lower proportion of *Nog^{mut}* NTOs contained any endpoint FOXA2$^+$ clusters compared with WT NTOs (Figure 4E). BMP4 treatment led to a further and dose-dependent reduction in the proportion of *Nog^{mut}* NTOs with any FOXA2$^+$ clusters (Figure 4E). Furthermore, when we quantified the size of FOXA2$^+$ clusters, *Nog^{mut}* NTOs and BMP-treated WT NTOs both exhibited significantly smaller FOXA2$^+$ clusters than untreated WT NTOs (Figure 4F). Exogenous application of NOGGIN protein to *Nog^{mut}* NTOs rescued the proportion of FOXA2$^+$ NTOs (Figure 4E) and FOXA2$^+$ cluster

pathway (GO: 0030509) based on Ensembl 94 annotation. Data point color indicates up-regulated in FOXA2$^+$ (green, #009988), up-regulated in FOXA2$^-$ (pink, #EE3377), or not significantly differentially regulated genes (light blue).
(D) Time course of NTOs fixed from days 3 to 5 (single z slice) showing a merged image at 10× magnification and a representative NTO (zoom) stained for DAPI (blue), FOXA2 (green), and LEF1 (left) or pERK (middle) or pSMAD1/5/9 (right) (magenta) to visualize WNT, FGF or BMP pathway activity respectively. Dashed white lines mark the outlines of the NTOs. Scale bars: 100 μm for 10× and 50 μm for zoom of representative NTOs.
(E) Analysis of Pearson correlation coefficient. Left: representative NTO used for the anti-correlation analysis performed on single z slices of images on day 5. For each NTO cross-section, a line with width of 10 pixels (shown in yellow) was drawn around the NTO, starting in the FOXA2$^+$ cluster and sparing the lumen. Scale bars, 100 μm. Right: intensity profiles of FOXA2 and LEF1/pERK/pSMAD were measured and analyzed by calculating the Pearson correlation coefficient by sampling the pixels for two channels (FOXA2 versus LEF1, FOXA2 versus pERK, FOXA2 versus pSMAD). NTOs are n = 56 LEF1, n = 49 pERK, n = 76 pSMAD. See also Figure S3.
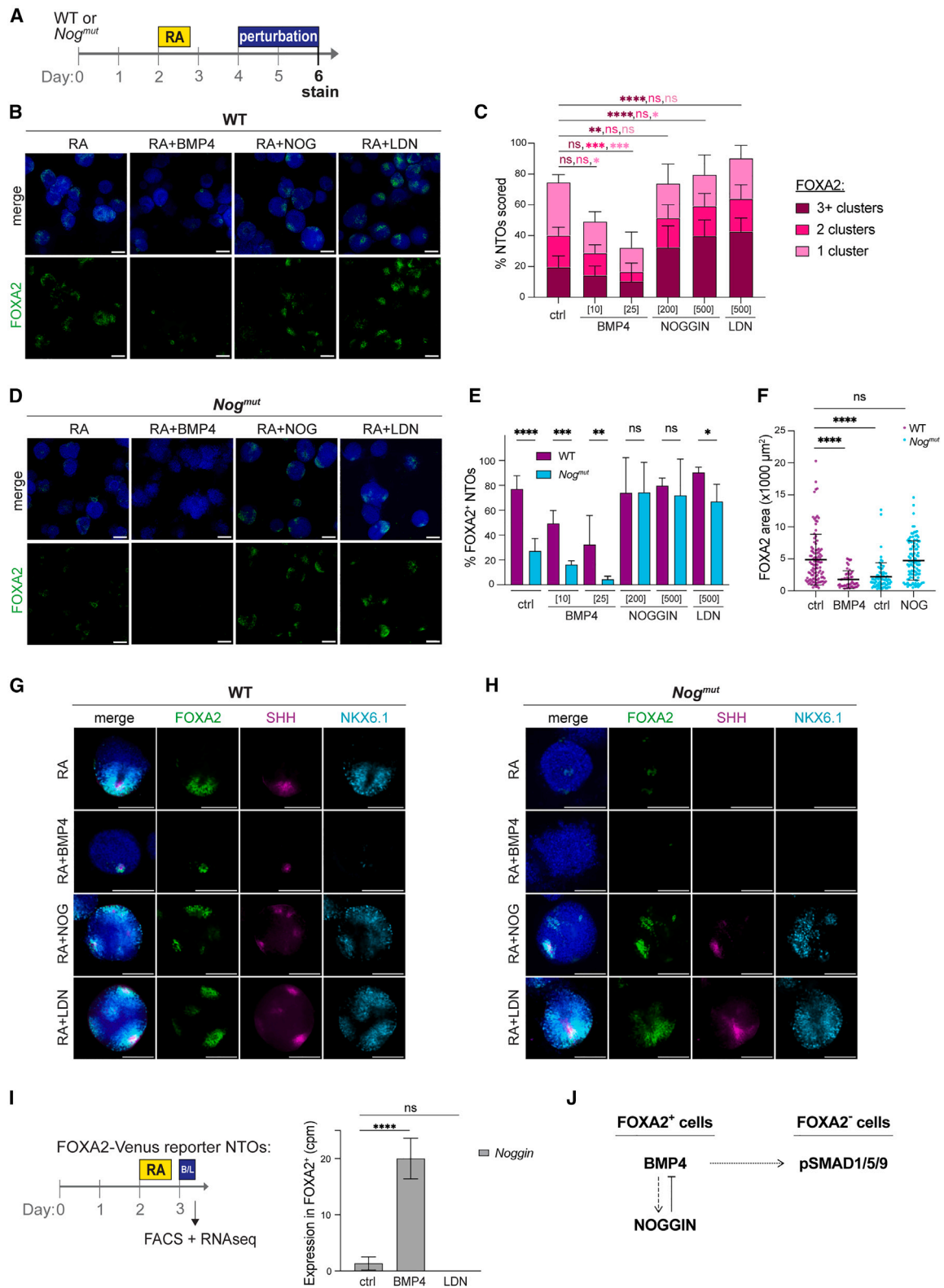
Figure 4. BMP pathway activation or suppression modulates FOXA2 cluster persistence

(A) Timeline of BMP pathway perturbations using "large NTO" protocol relevant for (B)–(H) (see Figure S4). Perturbations were performed from days 4 to 6 after an 18 h RA pulse from days 2 to 3.

(legend continued on next page)

size (Figure 4F) to WT levels. We confirmed that the FOXA2 clusters in NOGGIN-treated *Nog^mut* NTOs represent functional SHH-expressing floorplates at day 6 by co-staining for SHH and SHH/GLI-responsive NKX6.1 (Figures 4G and 4H).

Together, these data demonstrate that BMP signaling activity level regulates FOXA2⁺ cluster outcomes during NTO self-organization. BMP pathway activation versus inhibition controlled FOXA2⁺ cluster extinction versus persistence in a dose-dependent manner, as well as modulating FOXA2⁺ cluster size. Endogenously, *Bmp4* ligand and BMP-inhibitor *Noggin* were both expressed by FOXA2⁺ cells (Figure 3C), leading us to query the regulatory interactions between FOXA2, BMP4, and NOGGIN that underpin self-organization in NTOs. To examine how BMP signaling affects gene expression response in FOXA2⁺ cells, we perturbed the BMP pathway in NTOs, then sorted according to FOXA2-Venus reporter level and performed RNA-seq after 8 h to capture early transcriptional responses in nascent FOXA2⁺ cells (Figures 4I and S4I–S4K). FOXA2⁺ cells from BMP4-treated NTOs showed a significant increase in *Noggin* expression (Figure 4I), in agreement with BMP-driven *Noggin* induction reported in human two-dimensional (2D) gastruloids,[21] indicating a feedback loop in which FOXA2⁺ clusters protect themselves from the BMP ligands that they themselves produce (Figure 3C).

In summary, we propose a FOXA2-BMP4-NOGGIN signaling circuitry that underpins cluster competition during NTO self-organization (Figure 4J). FOXA2 cells express BMP ligands (Figure 3C) that, plausibly through pSMAD1/5/9, suppress FOXA2 in surrounding cells. NOGGIN, also expressed by FOXA2 cells (Figure 3C) and under feedback control by BMP (Figure 4J), promotes the persistence and size of winner clusters.

NOGGIN regulates floorplate size in the anterior NT *in vivo*

Given our observations in NTOs, we asked whether deleting *Noggin* might reduce floorplate size *in vivo*. We crossed mice bearing *Noggin* floxed (*Nog^Fl/Fl* or *Nog^Fl/+*)[22] and *Sox2^CreERT2/+* [23] alleles (Figures 5A and S5A), tamoxifen-treated at E5.5 to induce *Nog* conditional knockout (cKO) in the epiblast, and harvested embryos at E10.5 to evaluate FOXA2 and SHH expression in the NT at different anatomical levels (Figure 5B).

By quantifying the DAPI⁺ area in cross-sections, we observed that mutant embryos exhibited slightly smaller NTs in the cervical spine region compared with control embryos from the same developmental stage (Figure S5B). To avoid any confounding effect, we measured the areas of FOXA2 and SHH protein expression (Figures S5C and S5D), then normalized to respective NT size (Figure 5C). We found a significant decrease in the normalized areas of FOXA2 and SHH expression in *Nog* cKO compared with control embryos, specifically in the mid/hindbrain region in which the floorplate forms prior to notochord development.[24] By contrast, there was no difference in the FOXA2 and SHH domain sizes in the notochord-dependent cervical and thoracic spinal cord. Altogether, our *in vitro* and *in vivo* findings suggest that floorplate establishment in the mid/hindbrain region is regulated via BMP-dependent cell communication.

DISCUSSION

Here, we describe how a floorplate-signaling center self-organizes in clonal 3D NTOs. Following a pulse of RA signal, FOXA2⁺ cells emerge in a salt-and-pepper fashion at day 3,

(B) Representative images at 10× magnification (single *z* slice) of WT NTOs stained for DAPI (blue) and FOXA2 (green) for RA, RA + BMP4 (25 ng/mL), RA + NOG (200 ng/mL), and RA + LDN (500 nM). Scale bars, 100 μm.

(C) 3D analysis of numbers of FOXA2⁺ clusters in WT NTOs on day 6 shown in (B). Results were statistically analyzed using an ordinary one-way ANOVA and Dunnett's multiple comparisons test. For 3 or more clusters: RA versus RA + BMP4 (10 ng/mL) was n.s., RA versus RA + BMP4 (25 ng/mL) was n.s., RA versus RA + NOG (200 ng/mL) $p = 0.0029$, RA versus RA + NOG (500 ng/mL) $p \leq 0.0001$, RA versus RA + LDN (500 nM) $p \leq 0.0001$; for 2 clusters: RA versus RA + BMP4 (10 ng/mL) was n.s., RA versus RA + BMP4 (25 ng/mL) $p = 0.0005$, RA versus RA + NOG (200 ng/mL) was n.s., RA versus RA + NOG (500 ng/mL) was n.s., RA versus RA + LDN (500 nM) was n.s.; for 1 cluster: RA versus RA + BMP4 (10 ng/mL) $p = 0.0171$, RA versus RA + BMP4 (25 ng/mL) $p = 0.0007$, RA versus RA + NOG (200 ng/mL) was n.s., RA versus RA + NOG (500 ng/mL) $p = 0.0153$, RA versus RA + LDN (500 nM) was n.s. Concentration [x] expressed in ng/mL for BMP4 and NOGGIN, or in nM for LDN. Asterisks indicate statistical significance, n.s. indicates non-significance.

(D) Representative images at 10× magnification (single *z* slice) of *Nog^mut* NTOs stained for DAPI (blue) and FOXA2 (green) upon RA, RA + BMP4 (25 ng/mL), RA + NOG (200 ng/mL), and RA + LDN (500 nM). Scale bars, 100 μm.

(E) 3D analysis of the proportion of FOXA2⁺ NTOs shown in (B) and (D) of WT (purple) and *Nog^mut* (cyan). Results were statistically analyzed using an ordinary one-way ANOVA, always comparing WT with *Nog^mut* samples. RA versus RA $p \leq 0.0001$, RA + BMP4 (10 ng/mL) versus RA + BMP4 (10 ng/mL) $p = 0.0004$, RA + BMP4 (25 ng/mL) versus RA + BMP4 (25 ng/mL) $p = 0.0039$, RA + LDN (500 nM) versus RA + LDN (500 nM) $p = 0.0229$, while the other conditions were n.s. A total of $n = 3,407$ (between 306 and 414 per condition) WT NTOs and $n = 3,425$ (between 328 and 415 per condition) *Nog^mut* NTOs were included in the analysis. Concentration [x] expressed in ng/mL for BMP4 and NOGGIN, or in nM for LDN. Asterisks indicate statistical significance, n.s. indicates non-significance.

(F) 3D analysis of average surface area of FOXA2⁺ clusters in WT (purple) and *Nog^mut* (cyan) NTOs. Each dot represents an average cluster area in a given NTO. Results were statistically analyzed using Kruskal-Wallis test and Dunn's multiple comparisons test comparing RA with RA + BMP4 (in WT NTOs), RA and RA + NOG (in *Nog^mut* NTOs). WT RA versus WT RA + BMP4 $p \leq 0.0001$, WT RA versus *Nog^mut* RA $p \leq 0.0001$, and WT RA versus *Nog^mut* RA + NOG was n.s. Asterisks indicate statistical significance, n.s. indicates non-significance.

(G) Representative images (single *z* slice) of a day 6 WT NTO stained for DAPI (blue), FOXA2 (green), SHH (magenta), and NKX6.1 (cyan) for RA, RA + BMP4 (25 ng/mL), RA + NOG (200 ng/mL), and RA + LDN (500 nM). Scale bars, 100 μm.

(H) Representative images (single *z* slice) of a day 6 *Nog^mut* NTO stained for DAPI (blue), FOXA2 (green), SHH (magenta), and NKX6.1 (cyan) for RA, RA + BMP4 (25 ng/mL), RA + NOG (200 ng/mL), and RA + LDN (500 nM). Scale bars, 100 μm.

(I) Transcriptional response in FOXA2⁺ cells after BMP signal activation or suppression shows FOXA2⁺ cells induce *Noggin* expression after BMP exposure. Schematic: at day 3, BMP perturbations were added for 8 h before NTOs were dissociated and FACS sorted into FOXA2⁺ and FOXA2⁻ cells for RNA analysis. Expression levels (cpm) of *Noggin* in FOXA2⁺ cells upon RA, RA + BMP4 (1.5 ng/mL), and RA + LDN (100 nM) treatments. Results were statistically analyzed using DESeq2 with pairwise comparison, RA + BMP4 versus RA $p \leq 0.0001$ for *Noggin* expression. Asterisks indicate statistical significance, n.s. indicates non-significance.

(J) Model of conceptional interactions between BMP4 and NOGGIN activities in FOXA2⁺ cells and their interaction via pSMAD1/5/9 activity in FOXA2⁻ cells. See also Figure S4.
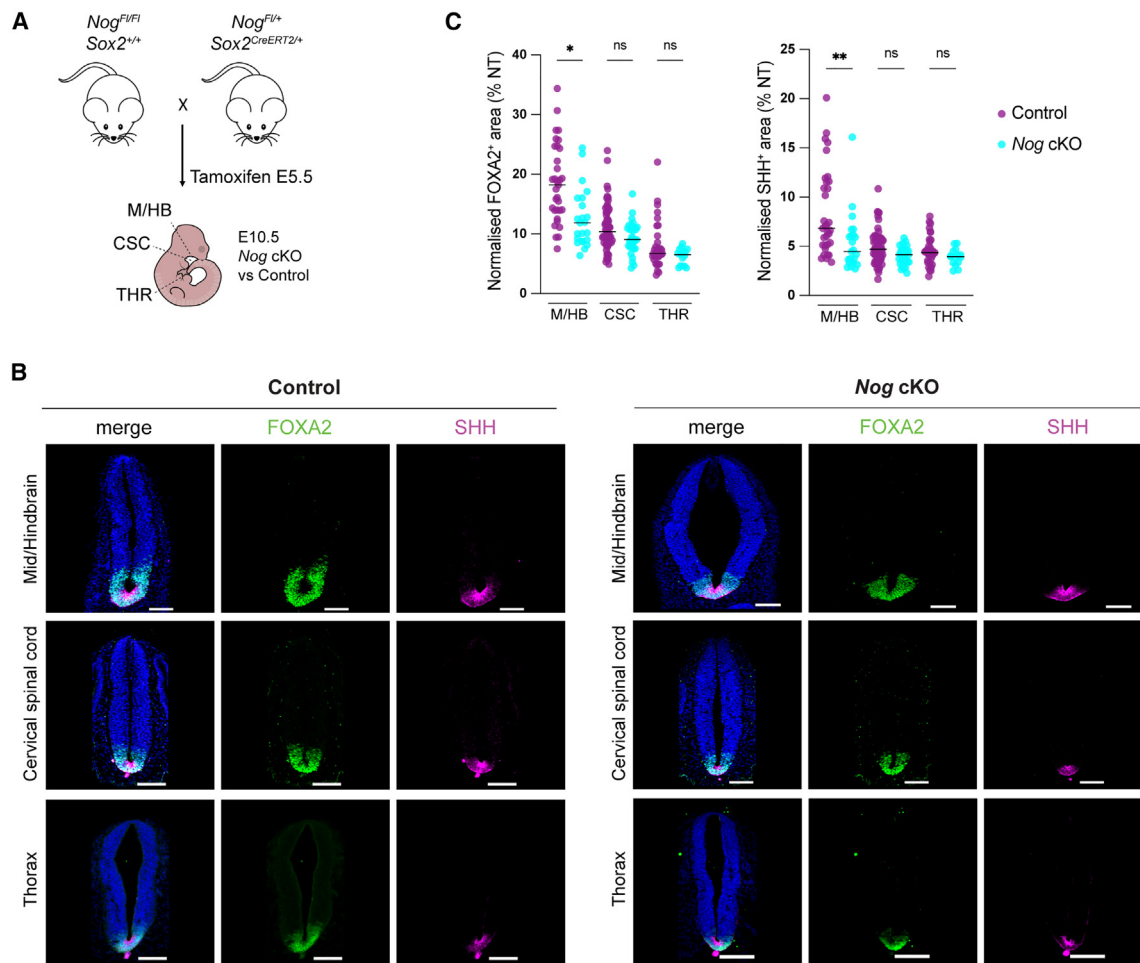
Figure 5. *In vivo* role of NOGGIN in anterior floorplate size in the mouse embryo

(A) Schematic of mouse crossing performed for inducible deletion of *Noggin*. E10.5 mouse showing the anatomy and section planes of the harvested and analyzed embryos.

(B) Representative images of E10.5 control (*Nog^{Fl/+};Sox2^{+/+}* or *Nog^{Fl/Fl};Sox2^{+/+}*) and *Nog* cKO (*Nog^{Fl/Fl};Sox2^{CreERT2/+}*) embryos of mid/hindbrain (M/HB), cervical spinal cord (CSC), and thorax (THR) regions stained for DAPI (blue), FOXA2 (green), and SHH (magenta). Scale bars, 100 μm.

(C) Normalized area of FOXA2 and SHH at different anterior-posterior levels of the embryonic NT. Quantification was made on serial sections of 6 control embryos (136 sections total, 33 for M/HB, 62 for CSC, 33 for THR) in purple and 3 *Nog* cKO embryos (68 sections total, 23 for M/HB, 30 for CSC, 15 for THR) in cyan from two litters. Kruskal-Wallis test and Dunn's multiple comparison tests were performed between anatomical regions of control versus *Nog* cKO (FOXA2: M/HB versus M/HB p = 0.0165, CSC versus CSC p = 0.2706, THR versus THR p = 0.3926, SHH: M/HB versus M/HB p = 0.0031, CSC versus CSC p = 0.0792, THR versus THR p = 0.4484). Horizontal bars represent means of the data, asterisks indicate statistical significance, n.s. indicates non-significance.

then undergo a process of cluster formation and resolution to form a localized domain in which SHH morphogen expression commences from day 5 (Figures 1 and 2). During NTO self-organization, intermediate FOXA2⁺ clusters do not behave independently but instead promote each other's extinction (Figure 2) via a BMP-mediated signaling mechanism, while NOGGIN protects FOXA2 (Figures 3 and 4). Furthermore, BMP4 application or *Noggin* mutation decreases FOXA2 domain size, which can be rescued by exogenous NOGGIN (Figure 4). Strikingly, the expression of both BMP ligands and inhibitors is enriched in FOXA2⁺ cells, whereas BMP signal transduction indicated by pSMAD1/5/9 is enriched in FOXA2⁻ cells (Figure 3). This represents a self-organization mechanism in which spatially scattered FOXA2⁺ cells express the signaling machinery driving their competition to result in a ventral pole.

We imaged this dynamic process and found that cells follow two major processes, cluster competition and cell sorting, which might be linked to a considerable heterogeneity in cluster size and FOXA2 expression level. Given that we identified the BMP4-NOGGIN circuit as a key player in cluster competition, we examined expression of these factors and saw correspondence with FOXA2 expression intensity. Correspondence between *Noggin* and FOXA2 first appeared in day 5 NTOs, while on day 4, *Noggin* expression was higher in FOXA2 low cells. It will be interesting to further understand whether this small, statistically significant difference in FOXA2 low cells on day 4 contributes to the dynamics of self-organization and whether heterogeneity in cluster size and brightness could relate to differential BMP circuit expression. Future work will be aimed at understanding cluster competition in NTOs more deeply, such as

how FOXA2 levels or cluster size are controlled, how the BMP-NOGGIN circuit interfaces with the sorting and differential cadherin expression, and whether one of these two processes might dominate over the other in different phases of the self-organization. Given the known tendency of cells to sort based on differential cadherin expression,[25] this observation may provide an explanation for the cell sorting observed in the NTOs. However, other recent advances have been reported to control floorplate formation in the mouse *in vivo* by integrating mechanical cues and translating these into cell-specific transcriptional programs, which could potentially also play a role in cell sorting of FOXA2 in the NTOs.[26]

Expression of both the FOXA2 "inhibitor" (BMP4) and "activator"/protector (NOGGIN) molecules from the same cells (FOXA2^{+}), and the feedback by which BMP4 promotes *Noggin* expression in FOXA2^{+} cells (Figure 4), displays features of a reaction-diffusion (RD) mechanism.[27] In the future, it will be interesting to test the extent to which an RD-type mechanism underpins floorplate patterning in NTOs. A thorough understanding will involve developing the means to determine the localization and dynamics of BMP pathway components. This NTO system offers the intriguing possibility to define, quantitatively, how the relative contributions of long-range communication versus physical cell sorting mechanisms (Figure 2) complement each other to promote self-organizational robustness. How our findings from mouse ESCs compare with recently described human NTOs that induce full or partial dorsoventral patterning will also be important.[28–30] In these studies, fixed time point analysis showed scattered FOXA2 prior to floorplate formation, but as less than 30% of human NTOs formed floorplates, it has been unclear whether the scattered starting point was an intermediate to the final state or whether distinct subpopulations arose over time.[28] WNT signaling has been proposed to act in an RD patterning system in human NTOs[30]—something that we did not observe in mouse NTOs. Whether these discrepancies are due to experimental approaches or whether they highlight intriguing inter-species differences remains to be addressed.

Other 3D organoid models that form from aggregates of 100s–1,000s of cells[31–35] can self-organize by amplifying initial asymmetries, yielding persistence of a signaling center at the location of its initial emergence. In contrast, our NTOs form clonally from single ESCs and show a regulative self-organization process, with nascent clusters competing via long-range signaling prior to establishing a stable ventral organizer. To our knowledge, cluster competition has not been observed in other organoid systems, although few studies have yet investigated the earliest stages of their self-organization due to constraints in efficiency, topographic predictability, or optical density that have limited tractability. Recent work addressing how 3D gastruloids initiate self-organization of an anterior-posterior axis[36,37] have combined improvements in homogeneity of input cells and analytical tools to elucidate how early variation in Nodal/BMP and cell position act prior to heterogeneity in WNT activity, which determines which cells will form the posterior pole, reinforced by cell sorting. Endogenous and exogenous BMP signaling have been shown to mediate organized lineage induction in 3D models of human epiblast[38,39] and mouse appendages,[40] but again without evidence of cluster competition. The processes we describe here are also distinct from those found in clonal in-

testinal organoids, where local activation of YAP1 induces symmetry breaking via DLL1 to determine the future crypt[41] without indication of competition between emergent DLL1 sites. An interesting question is whether mechanisms such as those we describe may be upstream of self-organization mechanisms in other organoids.

Here, we have identified and tested the importance of BMP signaling for cluster interactions in mouse NTOs. Because BMP is a key morphogen driving dorsal patterning of the NT from the dorsal roofplate organizer,[42–44] it seems surprising to observe BMP ligand expression in ventral floorplate cells. However, BMP ligands are reported to be expressed in the *in vivo* floorplate,[45–47] in keeping with the enrichment of BMP ligand expression we observe in FOXA2^{+} cells of NTOs (Figure 3). Our observation that BMP4 and NOGGIN regulate floorplate formation and size in NTOs led us to investigate whether BMP signaling circuitry plays a role in floorplate formation *in vivo*. cKO of *Noggin* in the epiblast led to a reduction in floorplate size at E10.5, particularly at mid/hindbrain regions of the NT where the floorplate, like our NTOs, forms in the absence of the underlying notochord (Figure 5). This raises the possibility that ventral sources of BMP may also contribute to NT patterning defects in mouse mutants of the BMP pathway.[45–47]

The broader applicability of the BMP-NOGGIN circuit regulating floorplate formation in NTOs highlights the potential of tractable *in vitro* self-organizing systems to uncover mechanisms that may contribute *in vivo*, by isolating or exaggerating such mechanisms away from the complexity of the developing embryo. This raises fascinating possibilities for the future: by integrating classical developmental biology with self-organization in stem cell models, we can quantitatively tease apart how embryonic context and inductive cues interface with self-organizing modules to allow regulative yet robust outcomes of vertebrate development.

Limitations of the study

In this study, we suggest differential cadherin expression as a possible explanation for the physical cell sorting of FOXA2^{+} cells occurring during self-organization. However, this might not be the only mechanism, and other (mechanical) cues could potentially contribute to cell sorting. When considering features that predict which cluster will win or lose during competition, we investigated cluster size and FOXA2 expression, but other parameters could also be involved. Additionally, we could not define the exact spatial localization of BMP4 and NOGGIN proteins due to the lack of functioning specific antibodies. Finally, the role of FOXA2^{−} cells in the self-organization process is still unknown.

STAR★METHODS

Detailed methods are provided in the online version of this paper and include the following:

- KEY RESOURCES TABLE
- RESOURCE AVAILABILITY
  - Lead contact
  - Materials availability
  - Data and code availability
- EXPERIMENTAL MODEL AND STUDY PARTICIPANT DETAILS

SUPPLEMENTAL INFORMATION

Supplemental information can be found online at https://doi.org/10.1016/j.devcel.2024.04.021.

AUTHOR CONTRIBUTIONS

T.K., H.T.S., and E.G. designed and performed experiments, created methodologies, and analyzed the data. K.I. provided supervision, set up live imaging conditions, developed image analysis pipelines, and helped to analyze data. D.C. and E.S. developed image analysis pipelines. M.M. and J.B. generated $Shh^{-/-}$ ESCs. F.B.P. performed and bioinformatically analyzed BRB sequencing. J.W. performed bioinformatic analyses. E.C. and L.A. performed experiments. S.L. and A.K. provided Nog cKO embryos. A.H. and R.A.N. assisted with the pharmacological screen. N.E. supported the development of larger NTO media. T.K., H.T.S., and E.M.T. wrote the manuscript. E.M.T. conceived and supervised the study.

REFERENCES

1. Spemann, H., and Mangold, H. (1924). über Induktion von Embryonalanlagen durch Implantation artfremder Organisatoren. Arch. f. Mikrosk. Anat. u. Entwicklungsmechanik *100*, 599–638. https://doi.org/10.1007/BF02108133.

2. Gurdon, J.B. (1987). Embryonic induction—molecular prospects. Development *99*, 285–306.

3. Martinez Arias, A., and Steventon, B. (2018). On the nature and function of organizers. Development *145*, dev159525. https://doi.org/10.1242/dev.159525.

4. Sato, T., Vries, R.G., Snippert, H.J., van de Wetering, M., Barker, N., Stange, D.E., van Es, J.H., Abo, A., Kujala, P., Peters, P.J., et al. (2009). Single Lgr5 stem cells build crypt-villus structures in vitro without a mesenchymal niche. Nature *459*, 262–265. https://doi.org/10.1038/nature07935.

5. Eiraku, M., Takata, N., Ishibashi, H., Kawada, M., Sakakura, E., Okuda, S., Sekiguchi, K., Adachi, T., and Sasai, Y. (2011). Self-organizing optic-cup morphogenesis in three-dimensional culture. Nature *472*, 51–56. https://doi.org/10.1038/nature09941.

6. Meinhardt, A., Eberle, D., Tazaki, A., Ranga, A., Niesche, M., Wilsch-Bräuninger, M., Stec, A., Schackert, G., Lutolf, M., and Tanaka, E.M. (2014). 3D Reconstitution of the Patterned Neural Tube from Embryonic Stem Cells. Stem Cell Reports *3*, 987–999. https://doi.org/10.1016/j.stemcr.2014.09.020.

7. Martyn, I., Kanno, T.Y., Ruzo, A., Siggia, E.D., and Brivanlou, A.H. (2018). Self-organization of a human organizer by combined Wnt and Nodal signalling. Nature *558*, 132–135. https://doi.org/10.1038/s41586-018-0150-y.

8. Bikoff, J.B., Gabitto, M.I., Rivard, A.F., Drobac, E., Machado, T.A., Miri, A., Brenner-Morton, S., Famojure, E., Diaz, C., Alvarez, F.J., et al. (2016). Spinal Inhibitory Interneuron Diversity Delineates Variant Motor Microcircuits. Cell *165*, 207–219. https://doi.org/10.1016/j.cell.2016.01.027.

9. Sagner, A., and Briscoe, J. (2019). Establishing neuronal diversity in the spinal cord: A time and a place. Development *146*, dev182154. https://doi.org/10.1242/dev.182154.

10. Dessaud, E., McMahon, A.P., and Briscoe, J. (2008). Pattern formation in the vertebrate neural tube: a sonic hedgehog morphogen-regulated transcriptional network. Development *135*, 2489–2503. https://doi.org/10.1242/dev.009324.

11. Le Dréau, G., and Martí, E. (2012). Dorsal-ventral patterning of the neural tube: A tale of three signals. Dev. Neurobiol. *72*, 1471–1481. https://doi.org/10.1002/dneu.22015.

12. Jessell, T.M. (2000). Neuronal specification in the spinal cord: inductive signals and transcriptional codes. Nat. Rev. Genet. *1*, 20–29. https://doi.org/10.1038/35049541.

13. Yamada, T., Placzek, M., Tanaka, H., Dodd, J., and Jessell, T.M. (1991). Control of cell pattern in the developing nervous system: Polarizing activity of the floor plate and notochord. Cell *64*, 635–647. https://doi.org/10.1016/0092-8674(91)90247-V.

14. Patten, I., Kulesa, P., Shen, M.M., Fraser, S., and Placzek, M. (2003). Distinct modes of floor plate induction in the chick embryo. Development *130*, 4809–4821. https://doi.org/10.1242/dev.00694.

15. Placzek, M., Tessier-Lavigne, M., Yamada, T., Jessell, T., and Dodd, J. (1990). Mesodermal Control of Neural Cell Identity: Floor Plate Induction by the Notochord. Science *250*, 985–988. https://doi.org/10.1126/science.2237443.

16. Placzek, M., and Briscoe, J. (2005). The floor plate: multiple cells, multiple signals. Nat. Rev. Neurosci. *6*, 230–240. https://doi.org/10.1038/nrn1628.

17. Kremnyov, S., Henningfeld, K., Viebahn, C., and Tsikolia, N. (2018). Divergent axial morphogenesis and early shh expression in vertebrate prospective floor plate. EvoDevo *9*, 4. https://doi.org/10.1186/S13227-017-0090-X/FIGURES/10.

18. Ranga, A., Girgin, M., Meinhardt, A., Eberle, D., Caiazzo, M., Tanaka, E.M., and Lutolf, M.P. (2016). Neural tube morphogenesis in synthetic 3D microenvironments. Proc. Natl. Acad. Sci. USA *113*, E6831–E6839. https://doi.org/10.1073/pnas.1603529113.

19. Ishihara, K., Mukherjee, A., Gromberg, E., Brugués, J., Tanaka, E.M., and Jülicher, F. (2023). Topological morphogenesis of neuroepithelial organoids. Nat. Phys. *19*, 177–183. https://doi.org/10.1038/s41567-022-01822-6.

20. Sasaki, H., Hui, C., Nakafuku, M., and Kondoh, H. (1997). A binding site for Gli proteins is essential for *HNF-3* β floor plate enhancer activity in transgenics and can respond to Shh in vitro. Development *124*, 1313–1322. https://doi.org/10.1242/dev.124.7.1313.

21. Etoc, F., Metzger, J., Ruzo, A., Kirst, C., Yoney, A., Ozair, M.Z., Brivanlou, A.H., and Siggia, E.D. (2016). A Balance between Secreted Inhibitors and Edge Sensing Controls Gastruloid Self-Organization. Dev. Cell *39*, 302–315. https://doi.org/10.1016/j.devcel.2016.09.016.

22. Stafford, D.A., Brunet, L.J., Khokha, M.K., Economides, A.N., and Harland, R.M. (2011). Cooperative activity of noggin and gremlin 1 in axial skeleton development. Development *138*, 1005–1014. https://doi.org/10.1242/dev.051938.

23. Arnold, K., Sarkar, A., Yram, M.A., Polo, J.M., Bronson, R., SenGupta, S., Seandel, M., Geijsen, N., and Hochedlinger, K. (2011). Sox2⁺ Adult Stem and Progenitor Cells Are Important for Tissue Regeneration and Survival of Mice. Cell Stem Cell *9*, 317–329. https://doi.org/10.1016/j.stem.2011.09.001.

24. Balmer, S., Nowotschin, S., and Hadjantonakis, A.-K. (2016). Notochord morphogenesis in mice: Current understanding & open questions. Dev. Dyn. *245*, 547–557. https://doi.org/10.1002/dvdy.24392.

25. Tsai, T.Y.C., Sikora, M., Xia, P., Colak-Champollion, T., Knaut, H., Heisenberg, C.P., and Megason, S.G. (2020). An adhesion code ensures robust pattern formation during tissue morphogenesis. Science *370*, 113–116. https://doi.org/10.1126/science.aba6637.

26. Cheng, C., Cong, Q., Liu, Y., Hu, Y., Liang, G., Dioneda, K.M.M., and Yang, Y. (2023). Yap controls notochord formation and neural tube patterning by integrating mechanotransduction with *FoxA2* and *Shh* expression. Sci. Adv. *9*, eadf6927. https://doi.org/10.1126/sciadv.adf6927.

27. Turing, A.M. (1952). The chemical basis of morphogenesis. Phil. Trans. R. Soc. Lond. B *237*, 37–72. https://doi.org/10.1098/rstb.1952.0012.

28. Zheng, Y., Xue, X., Resto-Irizarry, A.M., Li, Z., Shao, Y., Zheng, Y., Zhao, G., and Fu, J. (2019). Dorsal-ventral patterned neural cyst from human pluripotent stem cells in a neurogenic niche. Sci. Adv. *5*, eaax5933. https://doi.org/10.1126/sciadv.aax5933.

29. Abdel Fattah, A.R., Daza, B., Rustandi, G., Berrocal-Rubio, M.Á., Gorissen, B., Poovathingal, S., Davie, K., Barrasa-Fano, J., Cóndor, M., Cao, X., et al. (2021). Actuation enhances patterning in human neural tube organoids. Nat. Commun. *12*, 3192. https://doi.org/10.1038/s41467-021-22952-0.

30. Abdel Fattah, A.R., Grebeniuk, S., de Rooij, L.P., Salmon, I., Poovathingal, S., and Ranga, A. (2021). Neuroepithelial Organoid Patterning is Mediated by Wnt-Driven Turing Mechanism. Preprint at bioRxiv. https://doi.org/10.2139/ssrn.3811873.

31. Lancaster, M.A., Renner, M., Martin, C.-A., Wenzel, D., Bicknell, L.S., Hurles, M.E., Homfray, T., Penninger, J.M., Jackson, A.P., and Knoblich, J.A. (2013). Cerebral organoids model human brain development and microcephaly. Nature *501*, 373–379. https://doi.org/10.1038/nature12517.

32. Van Den Brink, S.C., Baillie-Johnson, P., Balayo, T., Hadjantonakis, A.-K., Nowotschin, S., Turner, D.A., and Martinez Arias, A. (2014). Symmetry breaking, germ layer specification and axial organisation in aggregates of mouse embryonic stem cells. Development *141*, 4231–4242. https://doi.org/10.1242/dev.113001.

33. Takata, N., Sakakura, E., Eiraku, M., Kasukawa, T., and Sasai, Y. (2017). Self-patterning of rostral-caudal neuroectoderm requires dual role of Fgf signaling for localized Wnt antagonism. Nat. Commun. *8*, 1339. https://doi.org/10.1038/s41467-017-01105-2.

34. Rivron, N.C., Frias-Aldeguer, J., Vrij, E.J., Boisset, J.C., Korving, J., Vivié, J., Truckenmüller, R.K., Van Oudenaarden, A., Van Blitterswijk, C.A., and Geijsen, N. (2018). Blastocyst-like structures generated solely from stem cells. Nature *557*, 106–111. https://doi.org/10.1038/s41586-018-0051-0.

35. Turner, D.A., Baillie-Johnson, P., and Martinez Arias, A. (2016). Organoids and the genetically encoded self-assembly of embryonic stem cells. BioEssays *38*, 181–191. https://doi.org/10.1002/bies.201500111.

36. McNamara, H.M., Solley, S.C., Adamson, B., Chan, M.M., and Toettcher, J.E. (2023). Recording morphogen signals reveals origins of gastruloid symmetry breaking. Preprint at bioRxiv. https://doi.org/10.1101/2023.06.02.543474.

37. Suppinger, S., Zinner, M., Aizarani, N., Lukonin, I., Ortiz, R., Azzi, C., Stadler, M.B., Vianello, S., Palla, G., Kohler, H., et al. (2023). Multimodal characterization of murine gastruloid development. Cell Stem Cell *30*, 867–884.e11. https://doi.org/10.1016/j.stem.2023.04.018.

38. Simunovic, M., Metzger, J.J., Etoc, F., Yoney, A., Ruzo, A., Martyn, I., Croft, G., You, D.S., Brivanlou, A.H., and Siggia, E.D. (2019). A 3D model of a human epiblast reveals BMP4-driven symmetry breaking. Nat. Cell Biol. *21*, 900–910. https://doi.org/10.1038/s41556-019-0349-7.

39. Shao, Y., Taniguchi, K., Townshend, R.F., Miki, T., Gumucio, D.L., and Fu, J. (2017). A pluripotent stem cell-based model for post-implantation human amniotic sac development. Nat. Commun. *8*, 208. https://doi.org/10.1038/s41467-017-00236-w.

40. Mori, S., Sakakura, E., Tsunekawa, Y., Hagiwara, M., Suzuki, T., and Eiraku, M. (2019). Self-organized formation of developing appendages from murine pluripotent stem cells. Nat. Commun. *10*, 3802. https://doi.org/10.1038/s41467-019-11702-y.

41. Serra, D., Mayr, U., Boni, A., Lukonin, I., Rempfler, M., Challet Meylan, L., Stadler, M.B., Strnad, P., Papasaikas, P., Vischi, D., et al. (2019). Self-organization and symmetry breaking in intestinal organoid development. Nature *569*, 66–72. https://doi.org/10.1038/s41586-019-1146-y.

42. Le Dréau, G., Garcia-Campmany, L., Rabadán, M.A., Ferronha, T., Tozer, S., Briscoe, J., and Martí, E. (2012). Canonical BMP7 activity is required for the generation of discrete neuronal populations in the dorsal spinal cord. Development *139*, 259–268. https://doi.org/10.1242/dev.074948.

43. Lee, K.J., Dietrich, P., and Jessell, T.M. (2000). Genetic ablation reveals that the roof plate is essential for dorsal interneuron specification. Nature *403*, 734–740. https://doi.org/10.1038/35001507.

44. Lee, K.J., Mendelsohn, M., and Jessell, T.M. (1998). Neuronal patterning by BMPs: a requirement for GDF7 in the generation of a discrete class of commissural interneurons in the mouse spinal cord. Genes Dev. *12*, 3394–3407. https://doi.org/10.1101/gad.12.21.3394.

45. Dale, K., Sattar, N., Heemskerk, J., Clarke, J.D.W., Placzek, M., and Dodd, J. (1999). Differential patterning of ventral midline cells by axial mesoderm is regulated by BMP7 and chordin. Development *126*, 397–408. https://doi.org/10.1242/DEV.126.2.397.

46. McMahon, J.A., Takada, S., Zimmerman, L.B., Fan, C.M., Harland, R.M., and McMahon, A.P. (1998). Noggin-mediated antagonism of BMP signaling is required for growth and patterning of the neural tube and somite. Genes Dev. *12*, 1438–1452. https://doi.org/10.1101/gad.12.10.1438.

47. Furuta, Y., Piston, D.W., and Hogan, B.L.M. (1997). Bone morphogenetic proteins (BMPs) as regulators of dorsal forebrain development. Development *124*, 2203–2212. https://doi.org/10.1242/DEV.124.11.2203.

48. Matsumoto, K., Mitani, T.T., Horiguchi, S.A., Kaneshiro, J., Murakami, T.C., Mano, T., Fujishima, H., Konno, A., Watanabe, T.M., Hirai, H., et al. (2019). Advanced CUBIC tissue clearing for whole-organ cell profiling. Nat. Protoc. *14*, 3506–3537. https://doi.org/10.1038/s41596-019-0240-9.

49. Nagy, A., Rossant, J., Nagy, R., Abramow-Newerly, W., and Roder, J.C. (1993). Derivation of completely cell culture-derived mice from early-passage embryonic stem cells. Proc. Natl. Acad. Sci. USA *90*, 8424–8428. https://doi.org/10.1073/pnas.90.18.8424.

50. Doetschman, T., Gregg, R.G., Maeda, N., Hooper, M.L., Melton, D.W., Thompson, S., and Smithies, O. (1987). Targetted correction of a mutant

CellPress
OPEN ACCESS

HPRT gene in mouse embryonic stem cells. Nature *330*, 576–578. https://doi.org/10.1038/330576a0.

51. Burtscher, I., Barkey, W., and Lickert, H. (2013). Foxa2-venus fusion reporter mouse line allows live-cell analysis of endoderm-derived organ formation. Genesis *51*, 596–604. https://doi.org/10.1002/dvg.22404.

52. Ran, F.A., Hsu, P.D., Wright, J., Agarwala, V., Scott, D.A., and Zhang, F. (2013). Genome engineering using the CRISPR-Cas9 system. Nat. Protoc. *8*, 2281–2308. https://doi.org/10.1038/nprot.2013.143.

53. Chu, V.T., Weber, T., Graf, R., Sommermann, T., Petsch, K., Sack, U., Volchkov, P., Rajewsky, K., and Kühn, R. (2016). Efficient generation of Rosa26 knock-in mice using CRISPR/Cas9 in C57BL/6 zygotes. BMC Biotechnol. *16*, 4. https://doi.org/10.1186/s12896-016-0234-4.

54. Schindelin, J., Arganda-Carreras, I., Frise, E., Kaynig, V., Longair, M., Pietzsch, T., Preibisch, S., Rueden, C., Saalfeld, S., Schmid, B., et al. (2012). Fiji: an open-source platform for biological-image analysis. Nat. Methods *9*, 676–682. https://doi.org/10.1038/nmeth.2019.

55. Stirling, D.R., Swain-Bowden, M.J., Lucas, A.M., Carpenter, A.E., Cimini, B.A., and Goodman, A. (2021). CellProfiler 4: improvements in speed, utility and usability. BMC Bioinformatics *22*, 433. https://doi.org/10.1186/s12859-021-04344-9.

56. Michlits, G., Jude, J., Hinterndorfer, M., De Almeida, M., Vainorius, G., Hubmann, M., Neumann, T., Schleiffer, A., Burkard, T.R., Fellner, M., et al. (2020). Multilayered VBC score predicts sgRNAs that efficiently generate loss-of-function alleles. Nat. Methods *17*, 708–716. https://doi.org/10.1038/s41592-020-0850-8.

57. Langmead, B., and Salzberg, S.L. (2012). Fast gapped-read alignment with Bowtie 2. Nat. Methods *9*, 357–359. https://doi.org/10.1038/nmeth.1923.

58. Love, M.I., Huber, W., and Anders, S. (2014). Moderated estimation of fold change and dispersion for RNA-seq data with DESeq2. Genome Biol. *15*, 550. https://doi.org/10.1186/s13059-014-0550-8.

59. Yu, G., Wang, L.-G., Han, Y., and He, Q.-Y. (2012). clusterProfiler: an R Package for Comparing Biological Themes Among Gene Clusters. Omics *16*, 284–287. https://doi.org/10.1089/omi.2011.0118.

60. Anders, S., Pyl, P.T., and Huber, W. (2015). HTSeq-A Python framework to work with high-throughput sequencing data. Bioinformatics *31*, 166–169. https://doi.org/10.1093/bioinformatics/btu638.

61. Shen, W., Le, S., Li, Y., and Hu, F. (2016). SeqKit: A Cross-Platform and Ultrafast Toolkit for FASTA/Q File Manipulation. PLoS One *11*, e0163962.

62. Martin, M. (2011). Cutadapt removes adapter sequences from high-throughput sequencing reads. EMBnet.journal *17*, 10. https://doi.org/10.14806/ej.17.1.200.

63. Haase, R., Royer, L.A., Steinbach, P., Schmidt, D., Dibrov, A., Schmidt, U., Weigert, M., Maghelli, N., Tomancak, P., Jug, F., et al. (2020). CLIJ: GPU-accelerated image processing for everyone. Nat. Methods *17*, 5–6. https://doi.org/10.1038/s41592-019-0650-1.

64. Berg, S., Kutra, D., Kroeger, T., Straehle, C.N., Kausler, B.X., Haubold, C., Schiegg, M., Ales, J., Beier, T., Rudy, M., et al. (2019). ilastik: interactive machine learning for (bio)image analysis. Nat. Methods *16*, 1226–1232. https://doi.org/10.1038/s41592-019-0582-9.

65. Mitchell, N.P., and Cislo, D.J. (2022). TubULAR: Tracking in toto deformations of dynamic tissues via constrained maps. Nat. Methods *20*, 1980–1988. https://doi.org/10.1101/2022.04.19.488840.

66. Rodolà, E., Bulò, S.R., and Cremers, D. (2014). Robust Region Detection via Consensus Segmentation of Deformable Shapes. Comput. Graph. Forum *33*, 97–106. https://doi.org/10.1111/cgf.12435.

67. Crane, K., Livesu, M., Puppo, E., and Qin, Y. (2020). A Survey of Algorithms for Geodesic Paths and Distances. Preprint at arXiv. https://doi.org/10.48550/ARXIV.2007.10430.

68. Baden, A., Crane, K., and Kazhdan, M. (2018). Möbius Registration. Comput. Graph. Forum *37*, 211–220. https://doi.org/10.1111/cgf.13503.

69. Lee, S.C., and Kazhdan, M. (2019). Dense Point-to-Point Correspondences Between Genus-Zero Shapes. Comput. Graph. Forum *38*, 27–37. https://doi.org/10.1111/cgf.13787.

70. Pallares, L.F., Picard, S., and Ayroles, J.F. (2020). TM3'seq: A Tagmentation-Mediated 3' Sequencing Approach for Improving Scalability of RNAseq Experiments. G3 (Bethesda) *10*, 143–150. https://doi.org/10.1534/g3.119.400821.

71. Hahaut, V., Pavlinic, D., Carbone, W., Schuierer, S., Balmer, P., Quinodoz, M., Renner, M., Roma, G., Cowan, C.S., and Picelli, S. (2022). Fast and highly sensitive full-length single-cell RNA sequencing using FLASH-seq. Nat. Biotechnol. *40*, 1447–1451. https://doi.org/10.1038/s41587-022-01312-3.

72. Alpern, D., Gardeux, V., Russeil, J., Mangeat, B., Meireles-Filho, A.C.A., Breysse, R., Hacker, D., and Deplancke, B. (2019). BRB-seq: ultra-affordable high-throughput transcriptomics enabled by bulk RNA barcoding and sequencing. Genome Biol. *20*, 71. https://doi.org/10.1186/s13059-019-1671-x.

73. Stottmann, R.W., Anderson, R.M., and Klingensmith, J. (2001). The BMP Antagonists Chordin and Noggin Have Essential but Redundant Roles in Mouse Mandibular Outgrowth. Dev. Biol. *240*, 457–473. https://doi.org/10.1006/dbio.2001.0479.

74. Pregizer, S.K., and Mortlock, D.P. (2015). Dynamics and Cellular Localization of *Bmp2*, *Bmp4*, and *Noggin* Transcription in the Postnatal Mouse Skeleton. J. Bone Miner. Res. *30*, 64–70. https://doi.org/10.1002/jbmr.2313.

75. Tate, M., Perera, N., Prakoso, D., Willis, A.M., Deo, M., Oseghale, O., Qian, H., Donner, D.G., Kiriazis, H., De Blasio, M.J., et al. (2021). Bone Morphogenetic Protein 7 Gene Delivery Improves Cardiac Structure and Function in a Murine Model of Diabetic Cardiomyopathy. Front. Pharmacol. *12*, 719290. https://doi.org/10.3389/fphar.2021.719290.

76. Truett, G.E., Heeger, P., Mynatt, R.L., Truett, A.A., Walker, J.A., and Warman, M.L. (2000). Preparation of PCR-Quality Mouse Genomic DNA with Hot Sodium Hydroxide and Tris (HotSHOT). BioTechniques *29*, 52–54. https://doi.org/10.2144/00291bm09.

STAR★METHODS

KEY RESOURCES TABLE

REAGENT or RESOURCE	SOURCE	IDENTIFIER
Antibodies		
Monoclonal rabbit anti-FOXA2	Cell Signalling Technologies	Cat# 8186; RRID:AB_10891055
Polyclonal goat anti-FOXA2	R&D	Cat# AF2400; RRID:AB_2294104
Monoclonal rabbit anti-SHH	Cell Signalling Technologies	Cat# 2207; RRID:AB_2188191
Monoclonal mouse anti-NKX6.1	DSHB	Cat# F55A10; RRID:AB_532378
Monoclonal rabbit anti-LEF1	Cell Signalling Technologies	Cat# 2230; RRID:AB_823558
Monoclonal rabbit anti-Phospho-SMAD1 (Ser463/465)/ SMAD5 (Ser463/465)/ SMAD9 (Ser465/467)	Cell Signalling Technology	Cat# 13820; RRID:AB_2493181
Monoclonal rabbit anti-Phospho-p44/42 MAPK (Erk1/2) (Thr202/Tyr204)	Cell Signalling Technology	Cat# 4370; RRID:AB_2315112
Monoclonal rabbit anti-E-Cadherin	Cell Signalling Technology	Cat# 3195; RRID:AB_2291471
Monoclonal rat anti-N-Cadherin	DSHB	Cat# MNCD2; RRID:AB_528119
Monoclonal mouse anti-ß-Tubulin	MPI-CBG	N/A
Alexa Fluor conjugated secondary antibodies for IHC (Donkey anti-Mouse/Goat/Rabbit)	Invitrogen	N/A
HRP conjugated secondary antibodies for WB (Goat anti-Rabbit/Mouse)	Invitrogen	N/A
DAPI	Sigma-Aldrich	Cat# D9542
Chemicals, peptides, and recombinant proteins		
N-2 Supplement (100X)	Gibco	Cat# 17502048
B-27™ Supplement (50X), serum free	Gibco	Cat# 17504044
DMEM/F-12, no glutamine	Gibco	Cat# 21331020
Neurobasal™ Medium	Gibco	Cat# 21103049
L-Glutamine (200 mM)	Gibco	Cat# A2916801
2-Mercaptoethanol (50 mM)	Gibco	Cat# 31350010
Penicillin-Streptomycin Solution	Gibco	Cat# 15140130
CHIR 99021	Tocris	Cat# 4423
PD 0325901	Tocris	Cat# 4192
Mouse LIF	Qkine	Cat# Qk018-1000
Accutase	Invitrogen	Cat# 00-4555-56
Sodium Pyruvate (100 mM)	Gibco	Cat# 11360070
BMP4	R&D	Cat# PHC9534
BMP7	R&D	Cat# 354-GMP
LDN-193189	Selleck Chemicals	Cat# S2618
Noggin	R&D	Cat# 6057-NG-025
FGF2	PeproTech	Cat# 100-18B
FGF8b	In house	N/A
IWP-2	Selleck Chemicals	Cat# S7085
IWR-1endo	Merck	Cat# I0161
Gelatin	Merck	Cat# G2500
Puromycin -dihydrochlorid	Thermo Scientific	Cat# P9620
Neomycin	Merck	Cat# N1142
Geneticin (G418)	Invivogen	Cat# ant-gn-1
Trypsin-EDTA (0.25%)	Gibco	Cat# 25200056
Albumin (BSA) Fraction V (pH 7.0)	Panreac AppliChem	Cat# A1391

Continued

REAGENT or RESOURCE	SOURCE	IDENTIFIER
Normal Donkey Serum	Jackson ImmunoResearch	Cat# 017-000-121
Target Retrieval Solution, Citrate pH 6	Dako	Cat# S2369
Advanced DMEM/F-12	Gibco	Cat# 12634010
MEM Non-Essential Amino Acids Solution (100X)	Gibco	Cat# 11140035
Basement Membrane Matrix (Matrigel)	Corning	Cat# BDL354234
CellCarrier-96 Ultra Microplates	PerkinElmer	Cat# 6055302
35 mm Dish | No. 1.5 Coverslip | 14 mm Glass Diameter | Uncoated	MatTek Corporation	Cat# P35G-1.5-14-C
All-Trans Retinoic Acid	Merck	Cat# R2625
Paraformaldehyde,reagent grade, crystalline	Merck	Cat# P6148
EMS 8% Paraformaldehyde Aqueous Solution, EM Grade	Electron Microscopy Sciences	Cat# 157-8
CUBIC-R+(N)	Matsumoto et al.[48]	N/A
Propyl gallate,for microscopy, $\geq$98.0% (HPLC)	Merck	Cat# 02370
Prolong™ Diamond Antifade Mountant	Invitrogen	Cat# P36965
Draq7™	Biostatus	Cat# DR71000
Rock inhibitor StemMACS Y27632	Miltenyi Biotec	Cat# 130-103-922
Tamoxifen	Sigma-Aldrich	Cat# T5648
TrypLE Select Enzyme (1X), no phenol red	Gibco	Cat# 50-591-419
NuPAGE 4-12% Bis-Tris gel	Invitrogen	Cat# NP0322BOX
Critical commercial assays		
RNeasy Mini Kit	Qiagen	Cat# 74104
DNase I	Qiagen	Cat# 79254
SuperScript VILO™ cDNA Synthesis Kit	Invitrogen	Cat# 11754050
Poly(A) mRNA Magnetic Isolation Module	New England Biolabs (NEB)	Cat# E7490
Ultra Directional RNA Library Prep Kit for Illumina	New England Biolabs (NEB)	Cat# E7420
HS RNA Kit	Agilent	Cat# DNF-472-0500
KAPA HiFi HS RM (100 x 25 rxns)	Roche	Cat# KK2601
Paramagnetic beads-based DNA purification Kit	In house	N/A
Recombinant RNasin(R) RNase Inhibitor, 2,500u	Promega	Cat# N2511
Maxima H Minus Reverse Transcriptase (200 U/L)	Thermo Scientific	Cat# EP0751
Exonuclease I (E.coli)	New England Biolabs (NEB)	Cat# M0293S
P3 Primary Cell 4D X Kit L (12 RCT)	Lonza	Cat# V4XP-3012
Deposited data		
RNA-Seq data related to Figure 3	This study	GEO: GSE221187
RNA-Seq data related to Figure 4	This study	GEO: GSE236543
RNA-Seq data related to Figure S5	This study	GEO: GSE260579
RNA-Seq data related to Figure S1	Ishihara et al.[19]	GEO: GSE214368
Experimental models: Cell lines		
Mus musculus (Male): R1	Nagy et al.[49]	Cat# SCRC-1011
Mus musculus (Male): HM1	Doetschman et al.[50]	N/A
FOXA2-Venus, H2A-mCherry (R1 background)	This study	N/A
Shh$^{-/-}$ (HM1 background)	This study	N/A
Nog^{mut} (R1 background)	This study	N/A
Experimental models: Organisms/strains		
Nog$^{tm1.1Rmh}$/J	Stafford et al.[22]	Strain #:016117, RRID:IMSR_JAX:016117
Sox2$^{tm1(cre/ERT2)Hoch}$/J	Arnold et al.[23]	Strain #:017593, RRID:IMSR_JAX:017593
Oligonucleotides		
gRNAs used in this study, see Table S1	Sigma-Aldrich	N/A

Continued

REAGENT or RESOURCE	SOURCE	IDENTIFIER
qPCR primers used in this study, see Table S1	Sigma-Aldrich	N/A
Genotyping primers used in this study, see Table S1	Sigma-Aldrich	N/A
Primers for cloning of FoxA2-Venus line, see Table S1	Sigma-Aldrich	N/A
Recombinant DNA		
FoxA2-Venus Fusion (FVF) E-85 plasmid	Burtscher et al.[51]	N/A
pSpCas9(BB)-2A-Puro (PX459)	Ran et al.[52]	Addgene plasmid #48139; RRID:Addgene_48139
pR26 CAG AsiSI/MluI	Chu et al.[53]	Addgene plasmid #74286; RRID:Addgene_74286
pR26-sA-DEST	This study	N/A
pR26-sA-H2-mCherry	This study	N/A
pSpCas9(BB)-2A-Puro (PX459) V2.0	Ran et al.[52]	Addgene plasmid #62988; RRID:Addgene_62988
U6-IT-EF1As-Cas9-P2A-GFP	This study	N/A
Software and algorithms		
Fiji/ ImageJ (v2.9.0)	Schindelin et al.[54]	https://imagej.net/software/fiji/
Jupyter lab (v3.4.8)	Jupyter	https://jupyter.org/
Python (v3.9.12)	Python	https://python.org/
R studio	R Core Team	https://www.R-project.org/
CellProfiler 4	Stirling et al.[55]	N/A
MATLAB R2021a	The MathWorks	N/A
GraphPad prism 9	Dotmatics	N/A
CRISPick	Broad Institute	https://portals.broadinstitute.org/gppx/crispick/public
VBC score	Michlits et al.[56]	https://www.vbc-score.org/
Bowtie 2 (v2.3.4.1)	Langmead and Salzberg[57]	https://bowtie-bio.sourceforge.net/bowtie2/index.shtml
STAR (v2.6.0c, v2.5.2a, v2.7.9a)	N/A	https://github.com/alexdobin/STAR
featureCounts subread (v1.6.2)	N/A	https://subread.sourceforge.net/
DESeq2 (v1.18.1, v1.26.0, v1.42.0)	Love et al.[58]	https://bioconductor.org/packages/release/bioc/html/DESeq2.html
Trim Galore (v0.5.0)	N/A	https://github.com/FelixKrueger/TrimGalore
GRCm38 genome (Ensembl release 94)	N/A	https://www.ensembl.org/Mus_musculus/Info/Index
Clusterprofiler 4.6.2	Yu et al.[59]	https://bioconductor.org/packages/release/bioc/html/clusterProfiler.html
UMI-tools (v1.0.0)	N/A	https://github.com/CGATOxford/UMI-tools
HTSeq (v0.11.2)	Anders et al.[60]	http://www-huber.embl.de/HTSeq
bcl2fastq	N/A	https://emea.support.illumina.com/sequencing/sequencing_software/bcl2fastq-conversion-software.html
SeqKit (v2.7.0)	Shen et al.[61]	https://bioinf.shenwei.me/seqkit/usage/
Cutadapt (v1.18)	Martin[62]	https://cutadapt.readthedocs.io/en/stable/
GO.db 3.16.0	N/A	https://bioconductor.org/packages/release/data/annotation/html/GO.db.html

RESOURCE AVAILABILITY

Lead contact
Further information and requests for resources and reagents should be directed to and will be fulfilled by the lead contact, Elly Tanaka (elly.tanaka@imba.oeaw.ac.at).

Materials availability
Reagents such as cell lines and plasmids generated in this study are available; requests for materials should be addressed to the lead contact.

Data and code availability

RNA-seq data generated in this study have been deposited at GEO under accession codes GSE221187 (FOXA2$^+$ versus FOXA2$^-$ cells at Day 5, Figure 3), GSE236543 (FOXA2$^+$ versus FOXA2$^-$ cells after BMP perturbations, Figure 4), and GSE260579 (RNA-seq of FOXA2$^-$ versus FOXA2$^+$ low, medium, high cells, Figure S4) and RNA-seq analyses are provided in Table S2.

This paper does not report original code.

Any additional information required to re-analyse the data reported in this paper is available from the lead contact upon request.

EXPERIMENTAL MODEL AND STUDY PARTICIPANT DETAILS

Cell culture

Cell lines

R1 mouse embryonic stem cell (ESC) line[49] was used for most experiments and as the parental line for FOXA2-Venus reporter and FOXA2-Venus and H2A-mCherry double-reporter generation, and for *Noggin* mutant (*Nog^mut*). HM1 ESC background[50] was used as the parental line for *Shh* knock-out (*Shh^-/-*). Cell lines were routinely tested and confirmed negative for mycoplasma.

Maintenance

ESCs were cultured in N2B27+2i+LIF (2iLIF) and incubated at 37°C in 5% CO$_2$. N2B27 medium comprised 1:1 DMEM/F-12 and Neurobasal (Gibco), 0.5% v/v N2 (Gibco), 1% v/v B27 (Gibco), 2 mM L-glutamine (Gibco), 1% penicillin/ streptomycin (Sigma), and 0.1 mM β-mercaptoethanol. To obtain 2iLIF medium, N2B27 was supplemented with 3 μM CHIR99021 (Tocris), 1 μM PD0325901 (Tocris) and 20 ng/ml murine LIF (Qkine). Tissue-culture treated 6-well plates were pre-coated with 0.15% gelatin (Sigma) in PBS at room temperature. Mouse ESCs were seeded at a density of 30,000 cells per 6-well, media was exchanged daily, and cells were passaged every third day by incubation with Accutase (Gibco) for 3 mins at 37°C, dissociation into single cells, centrifugation of the required number at 1,500rpm for 5 mins, then re-seeding in a fresh well.

Generation of reporter cell lines

Generation of FOXA2-Venus reporter ESCs. FoxA2-Venus Fusion (FVF) E-85 plasmid (kind gift from Heiko Lickert[51]) was used as a template for amplification of the FoxA2_exon3-venus-neo-PGK cassette, which was subsequently cloned into pGEMT-easy vector using Gibson Assembly technique. Two fragments for Gibson Assembly were amplified using the E-085 vector as a PCR template:

1) Fragment1 - "FoxA2_exon3-Venus-Neo":

GibAs_p3_fwd: CGGCCGCGGGGAATTCGATAAAGAATCAAAGACCAGTGGA
GibAs_p4_rev: GCCTCTCATTTCTACCGGGTAGGGGAGGCGCTTTT

2) Fragment 2 - "3' UTR-genomic DNA":

GibAs_p1_fwd: TCCCCTACCCGGTAGAAATGAGAGGCTGAGTGGAGACTTT
GibAs_p2_rev2: CGCGAATTCACTAGTGATTCCCTCCTCCTTCAATTTCTCTTCCTTGTGTT

For CRISPR/Cas9 mediated knock-in of the Venus sequence at the 3' end of the *FoxA2* gene locus, gRNA3 (GCCTGCTAGCTCTGGTCACTG) was cloned into the pSpCas9(BB)-2A-Puro (PX459) vector, containing the Cas9 sequence and a gRNA expression cassette. For *FoxA2* locus editing, both vectors were electroporated together into the ESC cell line R1 using the Amaxa Nucleofector 4D, program CG-104. 24 hours after the electroporation, G418 (100 μg/ml) was added to the culture medium to select for positive clones. Single clones were expanded, and correct integration of the Venus cassette was validated by PCR, sequencing and standard Western blot analysis.

In brief, protein of cell lysates was obtained by directly adding 5xSample Buffer and boiling samples at 95°C for 10 mins. The protein was loaded onto a NuPAGE™ 4-12% Bis-Tris gel (Invitrogen) and run for 20 mins at 100V, then 90 mins at 150V, then proteins were blotted onto a PROTRAN nitrocellulose transfer membrane (Whatman) by TE 77 Semi-Dry Transfer Unit (Amersham). The membrane was blocked in 5% BSA in 1x Transfer Buffer (10x TB, MeOH, H$_2$O) supplemented with Tween-20. Primary antibodies used: rabbit anti-FOXA2 (Cell Signalling Technologies, #8186S, 1:1000), and mouse anti-ß-tubulin (MPI-CBG antibody facility, 1:200), HRP-conjugated secondary antibodies used: Invitrogen Goat anti-Rabbit/Mouse 1:2000.

FoxA2_fwd5: GACCTCAAGGCCTACGAACA
Venus_rev2: GTTGTGGCGGATCTTGAAGT (Product size: 694bp)

Generation of FOXA2-Venus and H2A-mCherry double-reporter ESCs. H2A-mCherry was integrated into the Rosa26 safe harbour locus of FOXA2-Venus cell line. We first obtained a Rosa26 targeting vector with Puromycin selection cassette (pR26 CAG AsiSI/MluI, Addgene 74286, Ralf Kuehn lab, [53]), linearised the vector with SwaI restriction digest, and used Gibson Assembly to insert the Gateway destination sequence immediately 3' to the splice acceptor site, and created a new vector termed pR26-sA-DEST. Subsequently, we performed a Gateway LR reaction between pR26-sA-DEST and pME-H2A-mCherry to create pR26-sA-H2-mCherry. To edit the Rosa26 locus, we identified a new high efficiency guide RNA sequence ACTGGAGTTGCAGATCACGA (Rosa26-gRNA1), and co-transfected p-Rosa26-gRNA1 and pR26-sA-H2-mCherry to FOXA2-Venus cells with Amaxa nucleofection. After 24 hours, cells were selected with 1 μg/ml Puromycin and individual clones were expanded. Correct integration was confirmed by Sanger sequencing and the length of the PCR amplicon from two primers:

R26_leftout_fwd1: GCTTGGTGCGTTTGCGGGGGAT

mCherry_rev1: TTGGTCACCTTCAGCTTGGCG (Product size: 5943bp)

Generation of knockout and mutant mouse ESC lines by CRISPR/Cas9

gRNAs were designed using the following tools:

https://portals.broadinstitute.org/gppx/crispick/public or https://www.vbc-score.org/ [56]

Shh^{−/−}. A short guide RNA (sgRNA) sequence (GCTGCTGGTGTGCCCCGGGCTGG) was cloned into pSpCas9(BB)-2A-Puro (PX459) V2.0 (Addgene plasmid #62988) as outlined in Ran et al.[52] 2 µg of PX459 V2.0 containing the sgRNA sequence were electroporated into 2x10^{6} DVI2 ESCs (HM1 background) using program A023 of the Amaxa Nucleofector II (Lonza) to ablate endogenous *Shh* gene expression. Electroporated cells were seeded onto a gelatin coated 10cm CellBind plate and cultured in 2iLIF. The following day cells were treated with 1.5 µg/mL Puromycin (Sigma) for 48 hours. Cells were grown in 2iLIF until resistant colonies were ready to be picked. Single and well spaced-out colonies were picked using a 20 µl pipette tip, dissociated in 0.25% Trypsin (Gibco) and plated onto feeder cells in serum-containing ESC medium + LIF in a 96-well plate to allow expansion. Colonies were screened and confirmed for deletions via Sanger sequencing using primers ShhKOpFW (CAAGCTCTCCAGCCTTGCTA) and ShhKOpRV (CTGCTCCCGTGTTTTCCTCA). The 11bp deletion caused a frameshift and premature stop codon. Cell lines were adapted back to 2iLIF conditions.

Nog[mut]: sgRNA2 (GGCGGATGTGTAGATAGTGCTGG) was cloned into the U6-IT-EF1As-Cas9-P2A-GFP vector, containing the Cas9 sequence and a gRNA expression cassette. As described previously, ESCs (R1) were electroporated with the construct using the P3 Primary Cell 4D X Kit (Lonza) and Amaxa Nucleofector 4D (program CG-104). 40 hours post electroporation, single GFP^{+} cells were analysed and sorted based on their GFP expression relative to non-fluorescent control on a FACS Aria III machine into individual wells of 96-well plates and clonal lines were expanded. One clone was confirmed as trans-heterozygous mutant with a different sized deletion in each allele by PCR and sanger sequencing using the primers Nog_fwd1 TGAGGTGCACAGACTTGGAT and Nog_rev2 GCCGCCTTCCCAAGTAGA. CRISPR allele 1: large deletion followed by a frameshift and premature stop codon. 27 amino acids of NOGGIN protein remain, only corresponding to the signal peptide, followed by 21 out-of-frame amino acids. CRISPR allele 2: 33bp deletion including 8 amino acids of the signal peptide and 3 amino acids of NOGGIN.

Neural tube organoid (NTO) formation

ESCs were dissociated into single cells as described in "Maintenance". After centrifugation of the required number of ESCs in N2B27, the pellet was placed on ice then resuspended in Matrigel (Corning) to yield a suspension at 100 cells per µl of Matrigel. 45 µl of this suspension was spread evenly across a MatTek dish for FACS and RNA-seq experiments, or 4 µl of suspension was carefully distributed in the centre of an optical-bottom 96-well (PerkinElmer) for immunofluorescence experiments. Gellification was performed at 37°C for 15 mins (MatTek) or 4 min (96-well), then covered with pre-warmed N2B27 medium (2 ml per MatTek, or 100 µl per 96-well). "Standard" N2B27 medium for NTO generation was the same as the N2B27 base for 2iLIF (see "Maintenance"), with the addition of 1% sodium pyruvate (Gibco). "Advanced" N2B27 for making larger NTOs used Advanced DMEM/F-12 (Gibco 12634-010 instead of 21331-020) and was supplemented with 1% v/v non-essential amino acids (Gibco). In both cases, medium was exchanged daily from Day 2 onwards. On Day 2, 250 nM all-trans RA (Sigma) was added to the N2B27 medium, then removed after 18 hours. For perturbations to NTOs, the following proteins or small molecules were added at the concentrations indicated in the corresponding figures: BMP4 (Gibco), BMP7 (Gibco), LDN (Selleck Chemicals), NOGGIN (R&D), CHIR 99021 (Tocris), IWP-2 (Selleck Chemicals), IWR-1endo (Sigma), FGF2 (PeproTech), FGF8b (in house), or PD 0325901 (Tocris).

Mouse procedures

Mouse procedures were approved under the license BMWFW-66.018/0006-WF/V/3b/2016 ("Coordination of tissue growth and patterning in neural tube development") from the Austrian Bundesministerium für Wissenschaft, Forschung und Wirtschaft and performed in accordance with the relevant regulations. The following strains were previously described: *Sox2[CreERT2]*,[23] *Nog[Fl/+]*.[22] To conditionally delete *Noggin*, *Nog[Fl/+]* were bred to *Sox2[CreERT2]* mice to generate *Nog[Fl/Fl]*, *Sox2[CreERT2/+]* embryos. Pregnant mothers were intraperitoneally injected with 4mg tamoxifen in sunflower oil per mouse at embryonic Day E5.5. Embryos were harvested at E10.5. The expected ratios of genotypes were obtained.

METHOD DETAILS

Immunofluorescence
Wholemount staining of NTOs

NTOs were fixed in 2% PFA for 30 min at room temperature, by adding 1:1 volume of room temperature 4% PFA on top of culture media, to avoid Matrigel disintegration. After fixation, samples were washed three times in PBS, then blocked and permeabilised in b/p buffer (PBS, 1% BSA, 0.5% Triton X-100) for 24 hours at 4°C. Primary antibodies were applied in b/p buffer for 24-72 hours at 4°C to ensure deep penetration of the samples: LEF1 (Cell Signalling Technologies, #2230S, 1:200), FOXA2 (R&D, #AF2400, 1:400), FOXA2 (Cell Signalling Technologies, #8186S, 1:1000), NKX6.1 (DSHB, #F55A10s, 1:200). Samples were washed three times and for a total of at least 24 hours in b/p at 4°C, then incubated with Alexa Fluor conjugated secondary antibodies (Invitrogen Donkey anti-Mouse/Goat/Rabbit 1:400) and DAPI (Sigma) for 24-72 hours at 4°C. Finally, samples were washed then stored in PBS.

The following primary antibodies were also used with modifications to the fixation and staining procedures. For SHH (Cell Signalling Technologies, #2207S, 1:300), E-Cadherin (Cell Signalling Technologies, #24E10, 1:100) and N-Cadherin (DSHB, #MNCD2, 1:50), antigen retrieval with 1x citrate buffer (DAKO) was performed for 45 mins at 65°C prior to blocking and permeabilization. For

pSMAD1/5/9 (Cell Signalling Technologies, #13820S, 1:800), fixation was performed in EMgrade PFA (Electron Microscopy Sciences) (8% diluted to a 2% final concentration) (12mins for 4μl Matrigel at room temperature). For both pSMAD1/5/9 and pERK (Cell Signalling Technologies, #4370S, 1:500), after fixation samples were permeabilised with methanol for 10 mins at -20°C, then blocked in db/p (PBS, 5% donkey serum, 0.3% Triton X-100) at 4°C.

Optical clearing of wholemount NTOs
PBS was removed and CUBIC-R+(N) refractive index matching solution[48] was added to completely cover the samples and incubated for 30-60 min at RT. After this adaptation, CUBIC-R+(N) solution was exchanged to fresh CUBIC-R+(N) supplemented with 2 mg/ml propylgallate (Sigma) to reduce photobleaching.

Staining of embryo sections
E10.5 embryos were fixed on ice for 75 mins in 4% PFA, washed in PBS, then adapted to sucrose and embedded in gelatin prior to cryosectioning. Slides were washed 3x for 15 mins each in 41°C PBS to dissolve the gelatin. Afterwards, slides underwent antigen retrieval as per SHH staining protocol above, then were blocked for 1 hour at room temperature in b/p. Primary antibodies as above were incubated overnight at 4°C in a humidified chamber. Samples were washed 3x for 5 mins with PBS+0.3% Triton X-100 at room temperature. Secondary antibodies were applied in a concentration of 1:200 in b/p and incubated overnight at 4°C. Samples were washed 3x for 5 mins with PBS+0.3% Triton X-100 at room temperature, then mounted in ProLong Diamond Antifade Mountant.

Imaging
Viventis lightsheet live-imaging
ESCs were dissociated and seeded as described in "Neural tube organoid (NTO) formation", but at a density of 80 cells/μl Matrigel in special Viventis chambers, lined with FEP film from the inside. Chambers were manufactured manually by gluing the FEP sheet to the plastic chambers and left to dry overnight. Chambers were cleaned with plasma to reduce hydrophobic properties and facilitate the attachment of the Matrigel. Before use, chambers were washed 3x with water and 80% ethanol, and dried and sterilised under UV light for 1 hour at room temperature.

After seeding and gellification of 40 μl Matrigel, 1.5 ml of N2B27 medium was added to the chamber and exchanged daily from Day 2. Live-imaging was initiated from Day 3 of the NTO generation procedure, i.e. 6 hours after RA removal, over a timecourse of 48-75 hours. Samples were incubated at 37°C in 5% CO_2 with humidification throughout. Images were acquired using two Nikon 10x objectives (NA 0.3) for illumination and for detection one Nikon 25x (NA 1.1) water immersion objective with 18x magnification and imaged with the following settings: mCherry 50 ms exposure time, 0.5% laser power; Venus 10 ms exposure time, 3.5% laser power. Multiple NTOs at different *xyz* positions were imaged at each timepoint. Image acquisition was performed in stacks with 3 μm step size every 15 mins.

Spinning disk fixed sample imaging
Wholemount NTOs and embryo sections were imaged on a Spinning Disk Confocal Olympus (inverted) microscope using a 10x (NA 0.4) air objective. Lasers were used at 100% and exposure time was adjusted to 200 ms for all lasers. Resolution was 0.65 μm in *x* and *y*. For wholemount NTOs, 125 planes with 2 μm spacing in *z* were acquired to allow for 3D reconstruction, and an automated stage was used for high-throughput acquisition with unbiased selection of multiple positions per 96-well using a grid. For embryo sections, planes with 2 μm spacing in *z* were acquired. For von Mises-Fisher analyses, fixed NTO images were acquired on the same microscope but using a 40x (NA 1.25) silicon oil objective, with 0.57 μm spacing in *z*.

Image processing and quantification
The transition from the scattered FOXA2$^+$ state to the intermediate clustered state was scored manually in Figures 1D and 2C–2F. The transition is heterogeneous from NTO to NTO, and the tissue contains a high density of nuclei, so it was difficult to apply standardised parameters for automated image analysis. During manual analysis, a cluster was defined as at least three cells that were grouped together and displayed nuclear signal intensity of a minimum of 15% of Day 5 FOXA2 signal intensity.

Automated analyses were performed for Figures 1C, 4C, 4E, 4F, S1C, S2E, S3C, and S4C–S4E as described below.

Analysis of Viventis movies
As mentioned above, manual classification was performed to analyse data in Figures 2C–2F. To avoid biases, two people analysed two different datasets and confirmed findings from two different microscope methods with the same conclusion.

For intensity quantification of clusters over time in Figure 2D (right panel), we used maximum intensity *z*-projections, performed intensity-based thresholding for segmentation, and quantified the total FOXA2$^+$ intensity for each cluster for individual frames with a Python script using scikit-image library. The movies were manually inspected from an orthogonal view in the *x, z* plane to ensure that there were no clusters overlapping in the *z*-direction.

For presentation, representative maximum intensity *z*-projections were made in ImageJ,[54] or movies were exported as.mp4 files.

Analysis of fixed wholemount NTO images
Raw.vsi files were processed in ImageJ.[54] For presentation, single representative *z* slices were exported as.tif files with set display ranges for each channel and without any binning in *x-y*.

von Mises-Fisher analysis. Imaris software was used to 3D reconstruct and visualise each NTO. FOXA2$^+$ nuclei above a set intensity threshold were identified using the spots function in Imaris and applied as a batch script. The precision of automated FOXA2$^+$ nucleus identification was checked and corrected manually. The geometric centre of the inscribed spot was considered the geometric centre of each nucleus and their *x, y, z* coordinates were used to calculate the concentration parameter, *k*, as the resulting vector

calculated as a sum of all vectors built from the centre of the NTO to the centre of each FOXA2⁺ nucleus and normalised to the number of FOXA2⁺ nuclei.

Correlation analysis of FOXA2 versus LEF1, pERK, pSMAD1/5/9 signal intensities in NTOs. To analyse the spatial correlation of FOXA2 and signalling pathways, we used images of fixed NTOs prepared and acquired on the spinning disk microscope as described above. For each NTO, we used ImageJ[54] to visually determine the midsagittal plane, draw a curved path with linewidth of 10 pixel within the tissue, measured the intensities of different channels along this path, and exported the results. Then, we used a Python script to calculate the Pearson correlation between the FOXA2 channel and a second channel representing LEF1, pERK, or pSMAD1/5/9. In this way, we obtained a single Pearson correlation per NTO.

3D quantification of NTO features. For 3D image analysis, we first processed the raw.vsi files to isotropic.tif files using CLIJ[63] GPU-accelerated image processing library in ImageJ.[54] Due to the "fish-bowl" effect of CUBIC-R+(N)'s high refractive index (RI = 1.5), the effective z steps were 3 μm. We therefore binned images in x-y from 0.65 μm to 3 μm so that the 3D voxel dimensions were comparable (3 μm × 3 μm × 3 μm in the x, y and z directions).

To quantify FOXA2⁺ cluster number per NTO in 3D (Figures 4C, 4E, S4D, and S4E), we used CellProfiler 4.[55] First, we segmented the NTO outer boundary by applying Otsu thresholding to the z stacks from the DAPI channel. Then, we segmented FOXA2⁺ clusters by applying a set intensity threshold to the z stacks from the FOXA2 channel and assigned these "child" clusters to their "parent" NTO. The FOXA2 intensity threshold was determined by comparison between positive control RA-treated versus negative control untreated endpoint NTOs and applied equally across all samples from the same experiment.

For scoring whether NTOs expressed any FOXA2, NKX6.1 and/or SHH (Figures 1C and S1C) or E-/N-Cadherin (Figure S2E), the mean intensity of the corresponding channel was measured inside the DAPI segmented volume. To measure the size of NTOs (Figures S4C and S4E), the NTO surface area was inferred from the DAPI segmented volume assuming spherical shape and to overcome confounding crenulation of the mask surface.

Measurement of FOXA2⁺ cluster size and intensity. The quantification of FOXA2⁺ cluster properties was performed using tissue cartography, which is a framework for analysing the properties of tissue configurations that can be approximated as thin surfaces. First, down-sampled multi-channel image volumes were processed in Ilastik[64] to produce a high contrast segmentation of NTOs from background. Surface reconstruction methods contained in the TubULAR package[65] were then applied to these processed image volumes to build mesh triangulations approximating the epithelial mid-surface of each NTO. FOXA2 signal intensity on each NTO was quantified by evolving the mid-surface along the positive and negative normal directions to create a set of nested "onion layers" (Figure S2H). FOXA2 signal intensity was sampled at subpixel resolution onto mesh triangles of each onion layer. Values at the mid-surface were taken to be the maximum intensity projection of the values on all onion layers projected along the normal direction. Area-weighted averaging was used to compute a single intensity value for each mesh vertex from the associated values at sample points on adjacent mesh faces.

FOXA2⁺ clusters were identified on a per-vertex basis using a custom consensus clustering algorithm, which produces a single "best" clustering by comparing results across an ensemble of input clusterings. Prior to clustering, the FOXA2 intensity on each vertex was normalised between [0,1] by a linear re-scaling. For fixed wholemount images, this re-scaling was performed between the 5th and 95th percentiles of all raw intensities measured on all WT NTOs given the same RA treatment. For Viventis light sheet movies, this re-scaling was performed between the 5th and 95th percentiles of raw intensities from all time points measured from all NTOs visible in the same movie. A single clustering in the ensemble was generated by assigning an index to each vertex in the surface mesh using a modified k-means method. Given a set of random initial cluster centres, a modified version of Lloyd's algorithm was used to greedily minimise the following cost function:

$$C[\{\vec{c}\}, f_B] = \frac{1}{\sum_v a_v f_v} \left(\sum_{\vec{c_i} \in \{\vec{c}\}} \sum_{v \in \vec{c_i}} \frac{d^2(\vec{x_v}, \vec{c_i})}{D_{max}^2} a_v f_v + \alpha \sum_{v \in B} (f_v - f_B)^2 a_v f_v \right),$$

where $\{\vec{c}\}$ denotes the set of all cluster centers, f_B is the average FOXA2 intensity of the background, a_v is the barycentric area of vertex v, f_v is the normalised FOXA2 intensity on vertex v, $\vec{x_v}$ is the 3D location of vertex v, $d(\vec{x}, \vec{y})$ denotes the 3D Euclidean distance between two points $\vec{x}$ and $\vec{y}$ on the surface, D_{max} is the maximum distance between any two points on the NTO's surface, and α is a positive scalar that sets the relative weight of the foreground versus background terms in the cost function. The double sum in the first term runs over all vertices v associated to each cluster centre ($\vec{c_i} \in \{\vec{c}\}$). The sum in the second term runs over all vertices assigned to the background. A vertex v was assigned to cluster $\vec{c_i}$ if

$$d^2(\vec{x_v}, \vec{c_i}) < d^2(\vec{x_v}, \vec{c_j}) \quad \forall \, i \neq j \text{ and } d^2(\vec{x_v}, \vec{c_i}) < D_{max}^2 \, \alpha \, (f_v - f_B)^2, \text{ or alternatively to the background if}$$

$$D_{max}^2 \, \alpha \, (f_v - f_B)^2 < d^2(\vec{x_v}, \vec{c_i}) \quad \forall \, \vec{c_i} \in \{\vec{c}\}.$$

Intuitively, the cost function $C[\{\vec{c}\}, f_B]$ is minimised when all points in the background have similar (low) intensities and all foreground points are assigned to a nearby cluster centre. Given an ensemble of such clusterings, the method of Rodolà et al.[66] was used to produce a consensus clustering that is as close as possible to all the individual clusterings in the ensemble (Fréchet sample mean of the clustering ensemble). The consensus clustering was then post-processed to ensure that each FOXA2⁺ cluster was

connected. The use of a consensus clustering algorithm obviates the dependence of the output on the initial locations of the randomly chosen cluster centres. For given analysis, $\alpha = 1$ was set and 10 initial cluster centres were used to generate each element of the clustering ensemble. The initial background intensity was always taken to the lowest intensity on the surface. Numerical experiments showed that the choice of $d(\vec{x}, \vec{y})$ to be the 3D Euclidean distance produced indistinguishable results from more sophisticated methods using exact geodesic distances on the surface[67] after consensus clustering. Total FOXA2$^+$ surface area for a given NTO was taken to be the sum of all barycentric areas associated to each mesh vertex assigned to any FOXA2$^+$ cluster. For the quantification of FOXA2$^+$ cluster properties for fixed NTOs shown in Figure 4F, mean FOXA2$^+$ surface area per cluster was computed based on the number of FOXA2$^+$ clusters identified for each NTO.

For the Viventis light sheet movies, segmented clusters were tracked using a custom method. Care had to be taken to ensure that clusters could be tracked on the NTO surfaces as they grew and changed shape over time. NTO surfaces at subsequent time points were mapped to the unit sphere using the method of Baden et al.,[68] which constrains the mapping through a canonical centring of the scale factors, i.e. the ratio of the area of a local patch on the surface to the area of its image on the sphere. The final rotational degrees of freedom were registered by point matching sparse random subsets of vertices sampled from the mesh surfaces in the original data space. Numerical experiments demonstrated that more sophisticated methods involving optical flow (e.g. Lee and Kazhdan[69]) were not necessary. This correspondence constitutes a map $\Phi(t) : S_t \to S_{t+1}$, from the surface S_t at time t to the surface S_{t+1} at time $t + 1$, enabling us to follow the flow of material points on the surface over time. Clusters at subsequent time points were compared by measuring their mutual overlap and mutual distance. Explicitly, tracking backwards in time, the cost C_M of matching cluster i on surface S_t to cluster j on surface S_{t+1} was given by

$$C_M(i,j) = -\frac{\sigma_1 \left(\sum_{v \in i} 1_{P_j}(\Phi_t(v)) + \sum_{v \in j} 1_{P_i}(\Phi_t^{-1}(v)) \right)}{N_i + N_j} + \frac{\sigma_2}{2} \left(\frac{\sum_{v \in i} d(\Phi_t(v), P_j)}{N_i \, D_t} + \frac{\sum_{v \in j} d(\Phi_t^{-\epsilon}(v), P_i)}{N_j \, D_{t+1}} \right)$$

where $N_{(i,j)}$ is the number of vertices in cluster (i,j), $D_{(t,t+1)}$ is the average geodesic distance along the surface among all pairs of vertices on the mesh of $S_{(t,t+1)}$, $P_{(i,j)}$ denotes the surface patch corresponding to the respective cluster, $1_{P_{(i,j)}}(x)$ is the indicator function which is equal to 1 if the point $x \in P_{(i,j)}$ and 0 otherwise, and the $d(x, P_{(i,j)})$ denotes the minimum geodesic distance from the point x to any point in $P_{(i,j)}$. The sums run over all vertices v in the respective clusters. The constants σ_1 and σ_2 set the relative weights of the overlap and distance terms. Intuitively, C_M is small if the images of the clusters under the flow strongly overlap. Cluster i was matched to cluster j if the cost $C_M < C_U$, where C_U is some fixed cost for leaving a cluster unmatched. For all NTOs, we set $\sigma_1 = \sigma_2 = C_U = 1$. The tracking for all NTOs was then manually checked and curated using a custom-built GUI to ensure validity.

The result of the cluster tracking described above is a directed acyclic graph (DAG) for each NTO, where nodes in the graph represent a cluster at a particular time point and edges (always pointing from a cluster at time t to a cluster a time $t + 1$) describe the relationship between clusters at subsequent time points. The highly dynamic behaviour of clusters resulted in complex DAG topologies. DAGs were simplified by rejecting connected components that persisted for less than six hours and components that never achieved a minimum of 5% area fraction of the total NTO surface at any timepoint. Further simplification of the DAGs iteratively was achieved by merging simultaneous nodes in the block connected components of the corresponding undirected graph until only cut vertices remained. Branches that persisted for less than two hours simplified DAGs were rejected (Figure 2I). Extinction events that occurred during and after Day 4 were analysed. Features of both, "winning" (i.e. persisting) and "losing" (i.e. extinguished) clusters were averaged over the last hour prior to extinction (Figures 2G–2I; Table S1). Due to the high dynamicity of the clusters before this timepoint, categorisations were performed on a per NTO basis on simplified DAGs in Figure S2I.

Analysis of embryo sections

For area measurements of FOXA2 and SHH in embryo sections, we first converted raw.vsi files to maximum intensity z-projections in ImageJ.[54] We set all channels to auto intensity and used the freehand selection tool from ImageJ to outline 1) the outer edge of the NT based on DAPI staining, 2) the NT lumen, 3) FOXA2 signal, and 4) SHH signal, and measured area in μm^2. To get the actual area of the NT, we subtracted 1) NT area by 2) lumen area. To get the normalised area measurements of FOXA2 and SHH respectively, we divided the area measurement of the signal 3) or 4) by the NT area. For presentation, maximum intensity z-projections with set display ranges were used. We analysed 6 control and 3 cKO embryos from two litters.

RNA sequencing

RNA-seq data generated in this study are available at the Gene Expression Omnibus (GEO) under accession codes GSE221187 (FOXA2$^+$ versus FOXA2$^-$ cells at Day 5, Figure 3), GSE236543 (FOXA2$^+$ versus FOXA2$^-$ cells after BMP perturbations, Figure 4), and GSE260579 (RNA-seq of FOXA2$^-$ versus FOXA2$^+$ low, medium, high cells, Figure S4) and RNA-seq analyses are provided in Table S2.

RNA-seq of RA-treated versus untreated timecourse from day 2-5

Timecourse RNA-seq data[19] was obtained from GEO with accession code GSE214368 (related to Figure S1). In brief, RNA-seq reads were trimmed using Trim Galore (v0.5.0), filtered to remove abundant sequences using Bowtie 2 (v2.3.4.1),[57] aligned to the GRCm38 genome (Ensembl release 94) using STAR (v2.6.0c) and summarised per gene with featureCounts (subread v1.6.2). Further analysis was performed using DESeq2 (v1.18.1).[58]

RNA-seq of FOXA2$^+$ versus FOXA2$^-$ cells at day 5

RA-treated NTOs were extracted from Matrigel on day 5 (related to Figure 3), dissociated into single cell suspension and FACS sorted into two cell populations based on FOXA2-Venus expression relative to non-fluorescent control on a FACS Aria III machine. For each sample, produced in three biological replicates, a minimum of 50,000 cells was sorted for subsequent RNA extraction. RNA was extracted from sorted cells using QIAGEN RNeasy Micro Kit and then underwent library preparation using the NEBNext Poly(A) mRNA Magnetic Isolation Module (E7490) and the NEBNext Ultra Directional RNA Library Prep Kit for Illumina (E7420), and bulk RNA sequencing on an Illumina NextSeq500 (single-end reads 75bp).

RNA-seq reads were trimmed using Trim Galore (v0.5.0), filtered to remove abundant sequences using Bowtie 2 (v2.3.4.1),[57] aligned to the GRCm38 genome (Ensembl release 94) using STAR (v2.6.0c) and summarised per gene with featureCounts (subread v1.6.2). Further analysis was performed using DESeq2 (v1.18.1)[58] and activated and inhibited upstream regulators were predicted using IPA Upstream Regulator Analysis based on the differentially expressed genes.

Differentially expressed genes (DEG) of FOXA2$^+$ versus FOXA2$^-$ samples at a false discovery rate (FDR) threshold of 5% were subjected to IPA Upstream Regulator Analysis for predicting activated and inhibited upstream regulators. In addition, top 400 DEGs ranked by padj were used in gene set over-representation analysis with Clusterprofiler 4.6.2[59] and GO.db 3.16.0.

RNA-seq of FOXA2$^+$ versus FOXA2$^-$ cells after BMP perturbations

NTOs were treated with RA at Day 2 for 18 hours as usual. At Day 3, i.e. 6 hours after RA removal, BMP4 (1.5 ng/ml) or LDN (100 nM) was added for 8 hours (related to Figure 4). To harvest cells, NTOs were washed twice with ice cold PBS, then dissociated in TrypIE. FOXA2-Venus$^+$ or FOXA2-Venus$^-$ cells were FACS sorted into lysis buffer in a 96-well plate, with 100 cells sorted for each sample in triplicate, then snap frozen on dry ice. RNA was extracted and sequencing libraries were prepared following the TM3'seq protocol[70] for subsequent quantitative sequencing with enrichment for polyadenylated RNAs. Pooled libraries were sequenced on the Illumina NovaSeq S4 PE150 (paired-end 500bp reads).

The paired-end raw reads were first split and the 12bp of UMI were extracted from Read2 with UMI-tools (v1.0.0). Reads were then trimmed with Cutadapt (v1.18)[62] and mapped to the mouse genome (mm10) using STAR (v2.5.2a). UMI counts at gene levels were quantified by HTSeq (v0.11.2).[60] The normalised counts per million (cpm) were obtained with DESeq2 (v1.26.0).[58]

RNA-seq of FOXA2$^-$ versus FOXA2$^+$ low, medium, high cells

RA-treated NTOs were extracted from Matrigel, dissociated into single cell suspension and FACS sorted into four cell populations based on FOXA2-Venus expression relative to non-fluorescent control on a FACS Aria III machine, including Draq7 (Biostatus) staining to exclude dead/dying cells. For each sample, produced in four biological replicates, 10,000 cells were sorted for subsequent RNA extraction. RNA was extracted from sorted cells using QIAGEN RNeasy Micro Kit and quantified and checked for integrity using the Agilent DNF 472 HS RNA Kit RNA Kit for the fragment analyser. 40ng of RNA per sample was used to generate barcoded cDNA using a one-step RT-PCR reaction according to published protocols[71,72] using KAPA HiFi Hot Start Ready Mix (Roche) and Maxima H Minus reverse transcriptase (Thermo Fisher). The barcoded oligo dT primers include the sequence for the TN5 adapter A. After the reaction the samples were pooled and purified using an in-house paramagnetic beads-based DNA purification kit with a ratio of 0.8X to select for full length transcripts. Barcoded oligodT primers were removed by incubation with Exonuclease 1 (Thermo Fisher) followed by enzyme inactivation. 100ng of the resulting cDNA was tagmented using Tn5 coupled to the adapter B for 10 minutes at 55°C followed by Tn5 stripping with 0.2% SDS. Illumina Nextera XT adapters were added by PCR amplification of the tagmented cDNA using the KAPA HiFi plus dNTP's kit (Roche). The library was size selected using in-house paramagnetic beads with a right side selection ratio of 0.4X and a left side ratio of 0.7X, and subsequently sequenced on the Illumina NovaSeq S4 PE150 (paired-end 150bp reads).

Paired-end raw were demultiplexed from the rest of the sequenced libraries using bcl2fastq. Then reads were further demultiplexed with BRB-seq tools using the barcoded Read1, Read2 files corresponding to the cDNA sequences provided individually for each sample. The resulting reads were trimmed for adapters and polyA using Cutadapt (v1.18)[62] and paired using SeqKit (v2.7.0).[61] Reads were aligned into the mouse genome GRCm38 as well as demultiplexed using a white list of our sample barcodes and quantified using STARsolo (v2.7.9a). Differential gene expression analysis was performed with DESeq2 (v1.42.0) (related to Figure S4).[58]

RT-qPCR

RA-treated NTOs were extracted from Matrigel, dissociated into single cell suspension and FACS sorted into four cell populations based on FOXA2-Venus expression relative to non-fluorescent control on a FACS Aria. For each sample, produced in four biological replicates, 40,000 cells were sorted for subsequent RNA extraction. RNA was extracted from sorted cells using QIAGEN RNeasy Micro Kit and cDNA was prepared including random hexamers using the SuperScript VILO cDNA Synthesis Kit (Invitrogen), then diluted in a ratio of 1:5 for subsequent RT-qPCR analysis.

The following primers were used:

Noggin: fwd: TCAAAGGGCTGGAGTTCTCC, rev: TTACACACCATGCCCTCGG

Chordin[73]: fwd: CCAGAGCATCGCAGTTACAG, rev: TGTGGGATCTGTGAAACGAA

Bmp4[74]: fwd: TTCCTGGTAACCGAATGCTGA, rev: CCTGAATCTCGGCGACTTTTT

Bmp7[75]: fwd: GGCTGGCAGGACTGGATCAT, rev: GGCGCACAGCAGGGCTTGG

Genotyping

Lysates for PCR were prepared following the HotSHOT protocol.[76] Briefly, yolk sacs were transferred to clean tubes and lysed in Alkaline lysis reagent (25 mM NaOH, 0.2 mM disodium EDTA, pH 12) at 95°C for approx. 45 min. After cooling samples to 4°C, 1x volume of Neutralisation buffer (40 mM Tris-HCl, pH5) was added to stop the lysis reaction. 2 μl of lysate was used in a 20 μl PCR reaction. To genotype the Nog^{FL}, Primers Nog F 13351 (CCA CAA TAT CCA GCC CTT GT) and Nog R 13352 (AAG AGG CCC ATG TGA GTG TC) were used to detect the floxed allele. 10 μl PCR product was loaded onto a 2% gel and run at 110 Volt for 30 min. The WT band was 186bp, the mutant band 300bp. To genotype the $Sox2^{CreERT2}$, primers 344 (GTCCAATTTACTGACC GTACACC) and 345 (GTTATTCGGATCATCAGCTACACC), as well as the internal control primers OIMR0042 (CTAGGCCACAGAAT TGAAAGATCT) and OIMR0043 (GTAGGTGGAAATTCTAGCATCATCC) were used. The Mutant band was 705bp, the Internal Control 324bp.

QUANTIFICATION AND STATISTICAL ANALYSIS

Source data for each graph are provided in Table S1. Data of this study are presented as follows. Bar-plots with error bars showing standard deviation (SD): Figures 1C, 1E, 2E, 4C, 4E, 4I, S1A, S1C, S2E, S2G, S3C, and S4D. Box-plots with median represented as centre line, whiskers show range of values, dots (if present) represent all measurement points: Figures 1F, 3E, S1D, S2F, S4C, and S4E. Scatter dot-plots with mean represented as centre line (or dot) and error bars showing standard deviation (SD): Figures 4F, 5C, S4G, S5B, and S5C. Asterisks indicate statistical significance, n.s. indicates non-significance.